Coordination Chemistry Reviews 253 (2009) 2920–2934

Contents lists available at ScienceDirect

Coordination Chemistry Reviews

journal homepage: www.elsevier.com/locate/ccr

Review

Synthesis of multifunctional multiferroic materials from metalorganics

Manish K. Singh [a], Yi Yang [a], Christos G. Takoudis [a,b,*]

[a] Department of Chemical Engineering, University of Illinois, Chicago, IL 60607, United States
[b] Department of Bioengineering, University of Illinois, Chicago, IL 60607, United States

Contents

ARTICLE INFO

Article history:
Received 2 April 2009
Accepted 4 September 2009
Available online 9 September 2009

Keywords:
Multiferroics
MOCVD
ALD
CSD
Sol–gel
Precursors

ABSTRACT

Recent developments in the synthesis of multiferroic materials from metalorganics are reviewed. Single-phase multiferroics have weak coupling among ferroic properties. Heterostructures are more promising for device applications since the coupling in such structures is many orders of magnitude stronger. These heterostructures also offer more degrees of freedom such as composition, microstructure and orientation for optimized coupling. Two major deposition techniques are discussed: (i) metalorganic chemical vapor deposition (MOCVD), and (ii) chemical solution deposition (CSD). These techniques are versatile and economical for deposition of the mentioned structures. In MOCVD the film growth is continuous, whereas, CSD is a multi-step process that involves coating using suitable precursor solution followed by annealing in appropriate ambient, and the desired thickness is obtained by repeating these steps. The desired properties of metalorganic precursors suitable for use in these techniques are outlined. In the case of MOCVD, different precursor delivery methods for liquid and solid precursors are also presented as they are equally important. Recent efforts on fabrication of single-phase multiferroics and improvements in properties of single-phase materials through doping/substitution using MOCVD and CSD are reviewed. Formation and synthesis of multifunctional multiferroic composites and heterostructures using these techniques is an area that is still much to be explored.

1. Introduction

1.1. Multiferroic materials

Multiferroic materials exhibit at least two of the "ferroic" [1] properties—ferroelectricity, ferromagnetism, ferroelasticity and ferrotoroidicity—in the same phase [2,3] (Fig. 1). By combining these different physical properties in the *same* material, multiferroics offer a promising route to create multifunctional devices.

* Corresponding author at: Departments of Chemical Engineering and Bioengineering, University of Illinois at Chicago, 851 S. Morgan Street (M/C 063), Chicago, IL 60607, United States.
E-mail address: takoudis@uic.edu (C.G. Takoudis).

0010-8545/$ – see front matter © 2009 Elsevier B.V. All rights reserved.
doi:10.1016/j.ccr.2009.09.003

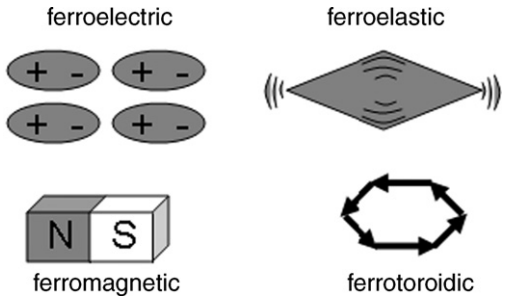

Fig. 1. The different forms of "ferroic" orders.

The current decade is witnessing a flurry of research activity on these materials and related phenomena (Fig. 2). Magnetoelectric (ME) multiferroics have drawn the most interest. They have both ferroelectric and ferromagnetic domains in the same phase with a coupling between them [4], and hence hold the promise to achieve the long sought-after combination of electronic and magnetic functionalities in a *single* device component. Realization of such devices would further advancements towards device miniaturization and better technology. High-speed low-power electrically controlled magnetic memory elements, electrically tunable microwave devices and highly sensitive magneto sensors are only a few of the vast array of aspired applications [5].

It was in early 1960s when the magnetoelectric coupling was first predicted and later observed in Cr_2O_3 [7,8]. The research on magnetoelectric materials continued for the next two decades before the excitement waned since not many such materials could be produced. However, recent developments in the field of materials research have led to renewed interest in multiferroic and magnetoelectric materials (Fig. 2). Improvements in first-principles theoretical calculations have provided us a better understanding of the underlying multiferroic phenomena at the atomic level [9,10] and have led to the identification of new mechanisms [11,12]. Similarly, the development of theory to describe the multiferroic effects in heterostructures has opened up another avenue for developing structures with stronger multiferroic effects [13]. This has given us the ability to design new multiferroic materials. Also, progress in thin film growth techniques has equipped us with capabilities to create new phases and modify existing materials [14]. The field

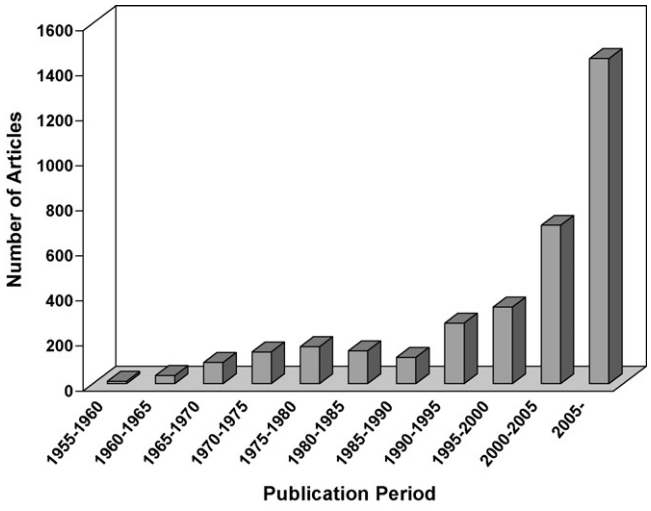

Fig. 2. Research activity on magnetoelectrics as indicated by the number of articles published during the last six decades. The data are based on analysis of search results obtained by specifying "magnetoelectric" as research topic search keyword in SciFinder Scholar [6].

of multiferroics has been progressing rapidly and there have been recent reviews covering this exciting research area [4,12,15–18].

In the subsequent sub-sections, this review will cover two broad categories of multiferroic structures: (i) single-phase compounds and (ii) heterostructures. Sections 2 and 3 would be devoted to the synthesis of these materials from metalorganic precursors. The desired properties of the metalorganic precursors would be discussed in Section 2 along with a review of available volatility and thermal stability data. Section 3 would focus on the reported efforts related to chemical vapor deposition and chemical solution deposition techniques for the synthesis of multiferroic structures employing different metalorganic precursors. Section 4 would summarize and conclude the review with an outlook to future developments.

1.2. Single-phase multiferroics

A major breakthrough in the understanding of the magnetoelectric effect came in the form of the pioneering work of Landau and Lifshitz wherein it was shown that the magnetoelectric response required a time-asymmetric media [19]. Experiments on Cr_2O_3, which was predicted to show such violation of time-reversal symmetry, constituted another major step forward in the research [8,20]. In the wake of the generated excitement, several more magnetoelectric compounds were identified [21]. However, the magnetoelectric coupling in the single-phase materials is too weak for application in devices, and can only be observed at very low temperatures because of their low Néel (T_N) and Curie (T_C) temperatures. The problem is further compounded by the fact that the single-phase magnetoelectric multiferroic materials are rare. This rarity has been explained through recent theoretical investigations [9,10]. The conventional atomic-level mechanisms that drive ferroelectricity in a material require empty transition metal orbitals, while those that drive ferromagnetism in a material require partially filled transition metal orbitals. Both these mechanisms are mutually exclusive. But, an alternate mechanism for driving either of these ferroic properties could lead to magnetoelectric behavior in a single-phase material [12,22,23]. A number of single-phase multiferroics that have been identified can be broadly classified into—(i) perovskites such as $BiFeO_3$, (ii) hexagonal manganites ($RMnO_3$, R = Y, Sc, In, Ho, Er, Dy, Tm, Yb, Lu), (iii) cuprates [24], and (iv) other compounds such as $BaMnF_4$ [25] and $Ni_3B_7O_{13}I$ [26]. Among these, $BiFeO_3$ deserves a special mention as it is the only known single-phase magnetoelectric material that has electric and magnetic ordering temperatures above room temperature (T_C ~1100 K and T_N ~650 K) [27].

1.3. Synthesized artificial multiferroic heterostructures

Apart from being rare and having very low Néel and/or Curie temperatures, the single-phase multiferroic compounds suffer from another major limitation. Since most of these compounds have definite compositions, the possibility of optimization of magnetoelectric property through ion substitution or doping is very limited [4]. Song et al. recently reported room temperature ferromagnetism and ferroelectricity in Co-doped $LiNbO_3$ films fabricated using laser beam epitaxy [28]. In the case of $BiFeO_3$, the use of dopants has been mainly driven by the idea that it would improve the ferroelectric properties by reducing the current leakage which is a major problem with $BiFeO_3$ films. Several reports have indicated that the dopants could affect the electrical properties of $BiFeO_3$ films via a structural modification such as reduced anisotropy, or by modifying the defect chemistry which controls the oxygen vacancies [29–32].

To explore new degrees of freedom for achieving stronger magnetoelectric coupling, the research has been directed towards

designing magnetoelectric materials. Fortunately, the timing seems to be good because recent progress in thin film deposition techniques has provided new routes to deposit novel multiferroics in the form of horizontal multilayer, vertical superstructures or other complex structures in a precise controlled manner [18,33]. One of the most promising approaches is to synthesize composites of magnetostrictive and piezoelectric materials [4]. The realization of the ME effect in this case can be represented as follows

$$\text{ME effect} = \frac{\text{magnetic}}{\text{mechanical}} \times \frac{\text{mechanical}}{\text{electrical}}$$

The concept was demonstrated in the pioneering works of van der Boomgaard and van Suchtelen on $CoFe_2O_4$–$BaTiO_3$ and $Ni(Co,Mn)Fe_2O_4$–$BaTiO_3$ composites [34,35]. In such composites the mechanical strain between the two materials is employed to induce the magnetoelectric effect. The ME effects in composites have been observed to be about hundred times greater than that in single-phase magnetoelectrics. However, the ME effect in this case may be non-linear unlike in the case of single-phase materials. Also, the interfacial mechanical strain should be transferred between the components with minimal losses. The related theory and experimental works have been reviewed in Refs. [4,36,37]. Based on this idea, one approach to obtain large magnetoelectric effects is to deposit thin films of a ferromagnet on a piezoelectric substrate such as lead magnesium niobate–lead titanate or $BaTiO_3$. If the strain transfer between the ferromagnet and the substrate is strong, an electrically applied strain in the substrate could induce strain in the ferromagnet film leading to the observation of magnetization changes. This indirect magnetoelectric effect could be due to stress-induced anisotropy or stress-induced phase changes. However, the substrate should have a large piezoelectric effect and at the same time should allow epitaxial growth of magnetic films for quantitative analysis [38]. Similarly, in the case of magnetic materials which have charge carrier density dependent magnetic properties, polarization of an adjacent ferroelectric film can control the magnetization near the interface.

2. Precursors

In this section, we discuss the desired properties of precursors so that they may be suitable for depositing films using metalorganic chemical vapor deposition (MOCVD) and chemical solution deposition (CSD). Although inorganic molecules may also be used for chemical vapor deposition and chemical solution deposition, they are beyond the scope of the present report. Since in the case of MOCVD, precursor delivery is as important as the choice of precursor itself, it would be discussed here briefly.

For application of MOCVD, availability of suitable precursors is critical. At the least the precursor: (i) should have a sufficiently high and reproducible vapor pressure, (ii) should not decompose during delivery or storage, and (iii) should not be hazardous [39]. Gas or liquid precursors with suitably high vapor pressures are ideal for MOCVD because of the ease with which they can be delivered to the reactor in a controlled manner. In the case of gas precursor, a mass flow controller is conventionally employed to control the dosage of precursor. For liquid precursors, the use of bubblers is the most dominant delivery method (Fig. 3). In such a setup, a carrier gas at a controlled flow rate is fed through the liquid in the bubbler so as to entrain the precursor molecules, thereby delivering the precursor to the reactor [40]. The bubbler has to be maintained at a specific temperature using a temperature controller in order to achieve a constant equilibrium precursor vapor pressure. Thus, in both cases, a simple and inexpensive arrangement is needed to reproducibly control the vapor phase concentration of the precursor in the reactor.

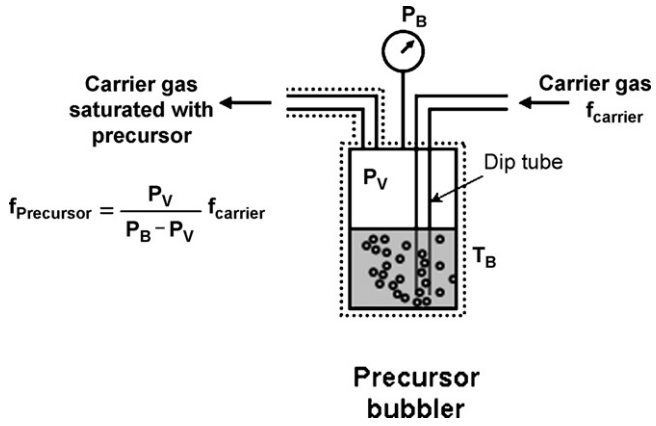

Fig. 3. Schematic of a precursor bubbler (dotted lines indicate heated sections). The carrier gas with a regulated flow rate ($f_{carrier}$) passes through the liquid precursor via a dip tube. The bubbler is kept at constant temperature (T_B) and pressure (P_B) to maintain constant precursor vapor pressure (P_V). The equation for estimating the flow rate of the precursor ($f_{precursor}$) is also shown.

On the other hand, solid precursors pose challenges that may limit their suitability for MOCVD. Solid precursors, in general, have relatively lower vapor pressures compared to liquids. More importantly, their vapor pressures decrease because of changing surface area as they are consumed. Also, lower vapor pressures require that solid precursors be used at elevated temperature to increase the vapor pressure; but this could lead to agglomeration and/or degradation of the precursor in the precursor vessel. However, for many metals, only solid precursors are available. Therefore, in order to overcome these difficulties with solid precursors, ingenious yet complex and expensive non-conventional delivery approaches have been developed which would be discussed in Section 3.

Table 1 lists the metalorganic precursors that have been reported for chemical vapor deposition of $BiFeO_3$ and other multiferroics. Their structures are shown in Figs. 4–6. β-Diketonates have been more popular than any other class of volatile precursors for chemical vapor deposition of multiferroics. This may be credited to the extensive studies on the chemistry of these complexes to understand the fundamental relationships between their volatility and their structure [41,42]. Their volatility depends strongly on the degree of branching of the hydrocarbon end groups as they largely determine the strength of the intermolecular interactions. The branching increases their volatility and decreases their tendency to hydrate or polymerize. The volatility also depends on the nature of the complex-forming metal. In case of rare-earth β-diketonates, the volatility increases in the series from La to Lu which has been attributed to the lanthanide contraction [43]. For Bi, aryl sources, particularly triphenyl bismuth, have been equally popular because of their good thermal stability upon sublimation and during storage [44]. In case of iron precursors, metallocenes have been the other major choice apart from the β-diketonates.

The volatility and thermal stability during evaporation are critical properties that determine the suitability of a precursor for MOCVD. The vapor pressure of precursors reported for MOCVD of multiferroic materials is presented in Table 2. A good thermal stability ensures that the precursor would neither decompose while flowing through the delivery lines nor would it degrade during storage. In order to use a precursor efficiently, it should evaporate completely without leaving any residue. When depositing a multi-metal oxide more than one metalorganic precursor is required, therefore, it becomes important that their volatilities be similar when using a liquid injection type of delivery scheme. To characterize these properties, thermogravimetric (TG) analysis, differential scanning calorimetry, mass spectroscopy and infrared spectroscopy techniques are most appropriate [64].

Table 1
Combinations of precursors reported for MOCVD of single-phase multiferroic materials.

Deposited material	Synthesis	Precursors	Reference
$BiFeO_3$	MOCVD	$Bi(Me)_2$(dmamp); $Fe(EtCp)_2$	[45]
	DLI-MOCVD	$Bi(thd)_3$; $Fe(thd)_3$	[46]
	DLI-MOCVD	$Bi(p\text{-tol})_3$; $Fe(DIBM)_3$	[47]
	DLI-MOCVD	$Bi(thd)_3$; $Fe(thd)_3$ $Bi(mmp)_3$; $Fe(thd)_3$	[48]
	Solid feeder MOCVD	$Bi(Ph)_3$; $Fe(thd)_3$	[49]
	MOCVD	$Bi(Ph)_3$; Fe(*n*-BuCp)(Cp)	[50]
$YMnO_3$	MOCVD	$Y(thd)_3$; $(MeCp)Mn(CO)_3$	[51]
	MOCVD	$Y(thd)_3$; $Mn(thd)_3$	[52]
	DLI-MOCVD	$Y(thd)_3$; $Mn(thd)_3$	[33,53]
$HoMnO_3$	MOCVD	$Ho(thd)_3$, $Mn(thd)_3$	[52]
	DLI-MOCVD	$Y(thd)_3$; $Mn(thd)_3$	[33]
$DyMnO_3$	MOCVD	$Dy(thd)_3$; $Mn(thd)_3$	[52,54]
	DLI-MOCVD	$Dy(thd)_3$; $Mn(thd)_3$	[33]
$TbMnO_3$	DLI-MOCVD	$Tb(thd)_3$; $Mn(thd)_3$	[33]
$ErMnO_3$	DLI-MOCVD	$Er(thd)_3$; $Mn(thd)_3$	[55]
$Pr_{(1-x)}Ca_xMnO_3$	DLI-MOCVD	$Pr(thd)_3$; $Ca(thd)_2$; $Mn(thd)_3$	[56]

dmamp: 2-[(dimethylamino-*N*)methyl]phenyl; Cp: cyclopentadienyl; Ph: phenyl; thd: 2,2,6,6-tetramethyl-3,5-heptanedionato; DIBM: diisobutyrylmethanato; mmp: 1-methoxy-2-methyl-2-propoxide.

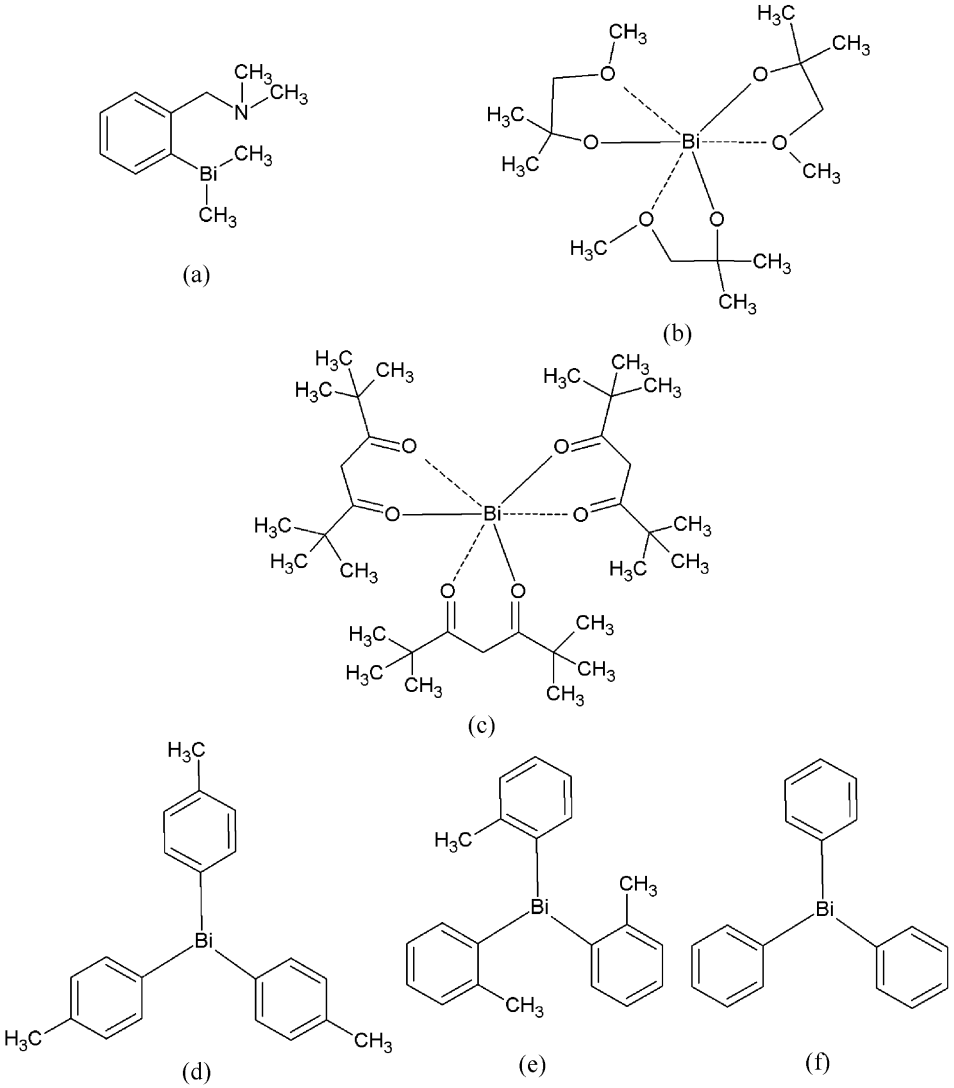

Fig. 4. Structures of bismuth metalorganic precursors that have been reported for MOCVD of $BiFeO_3$. (a) $Bi(dmamp)(Me)_2$, (b) $Bi(mmp)_3$, (c) $Bi(thd)_3$, (d) $Bi(p\text{-tol})_3$, (e) $Bi(o\text{-tol})_3$, (f) $Bi(Ph)_3$.

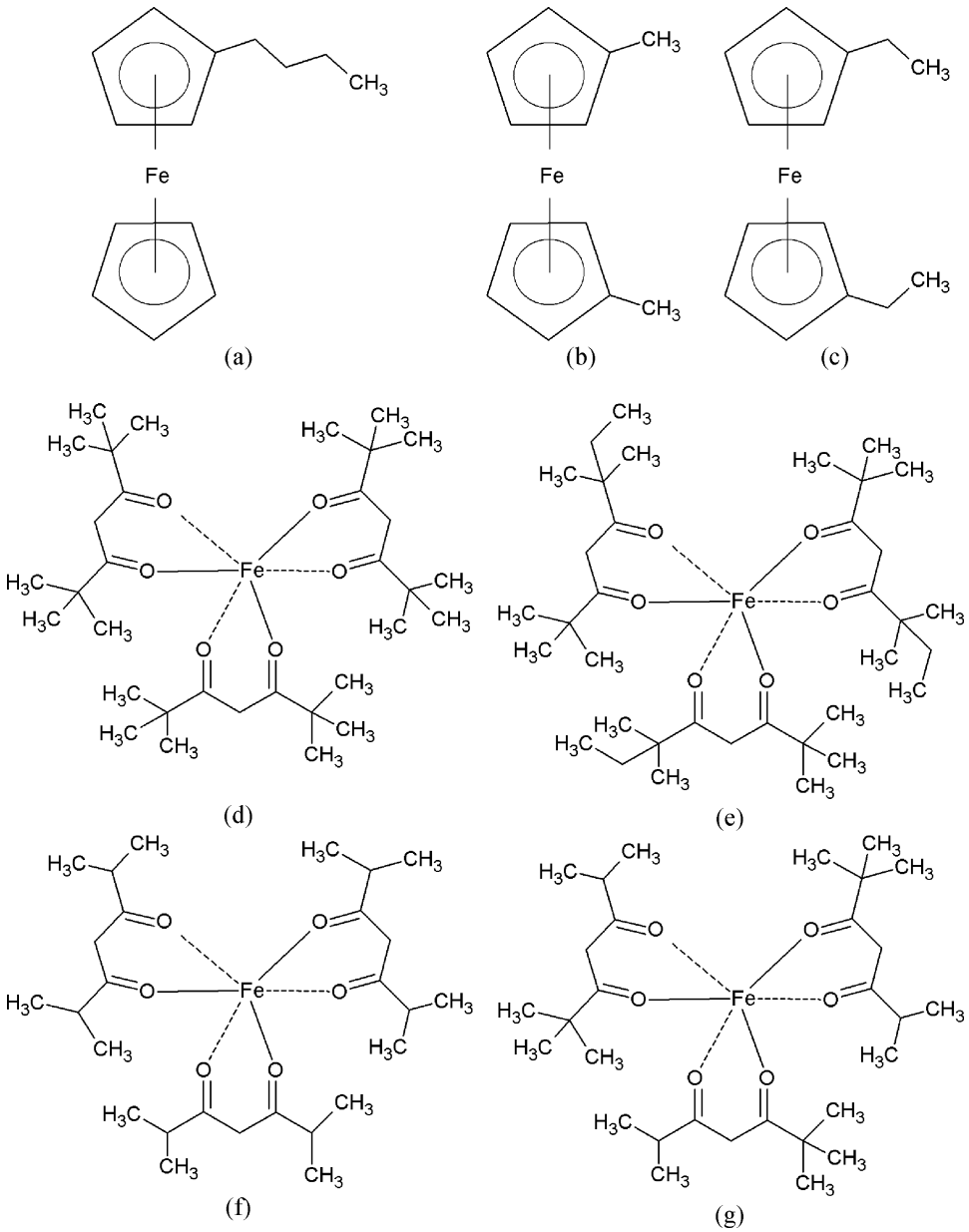

Fig. 5. Structures of iron metalorganic precursors that have been reported for MOCVD of $BiFeO_3$. (a) Fe(*n*-BuCp)(Cp), (b) $Fe(MeCp)_2$, (c) $Fe(EtCp)_2$, (d) $Fe(thd)_3$, (e) $Fe(TMOD)_3$, (f) $Fe(DIBM)_3$, (g) $Fe(IBPM)_3$. TMOD: 2,2,6,6-tetramethyl-3,5-octanedionato; IBPM: isobutyrylpivaloylmethanato.

The thermal behavior of $Bi(Ph)_3$ has been characterized by thermogravimetric analysis [65] and it was observed that $Bi(Ph)_3$ vaporized in a single step without any decomposition. The vaporization occurs in the range 160–280 °C with a final residue of about 5% at 350 °C. Bi(*o*-tol)$_3$ and Bi(*p*-tol)$_3$ which belong to the same class as $Bi(Ph)_3$ also show similar thermal characteristics. Based on the reported TG analysis Bi(*o*-tol)$_3$ and Bi(*p*-tol)$_3$ undergo single step clean evaporation in the range 170–350 °C and 170–300 °C, respectively [44]. The final residue left at 600 °C was 3.3 % and 1.4 %, respectively. Interestingly, in situ infrared spectroscopy indicate that during MOCVD Bi(*p*-tol)$_3$ dissociated via a different mechanism than Bi(*o*-tol)$_3$. While the *ortho* derivative dissociates via a breakdown of the aromatic rings, in case of the *para* derivative the breakdown involves dissociation of the aromatic ring-methyl bond. Thermogravimetric analysis curve for $Bi(thd)_3$ reveals two mass losses in the ranges 80–190 °C and 190–310 °C [44]. The final residue was reported to be 2.29%. Mass spectrometry analysis performed on the vapors produced during the thermogravimetric

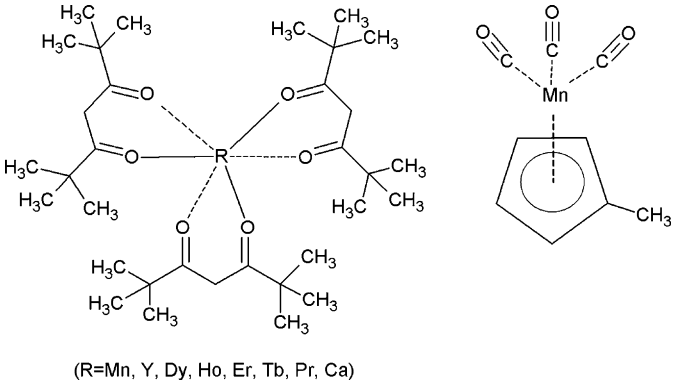

Fig. 6. Structures of metalorganic precursors that have been reported for MOCVD of manganites.

Table 2
Vapor pressure data of precursors reported for MOCVD of single-phase multiferroic materials.

Precursor	Vapor pressure	Temperature range (K)	Reference
$Bi(Ph)_3$	$\log_{10} p(\text{Torr}) = 11.19 - \frac{4885}{T(\text{K})}$	353–473	[57]
$Bi(o\text{-tol})_3$	$\log_{10} p(\text{Torr}) = 13.45 - \frac{6267}{T(\text{K})}$	–	[58]
$Fe(Cp)_2$	$\log_{10} p(\text{Torr}) = 10.66 - \frac{3805}{T(^\circ\text{C})+273.15}$	295–325	[59]
$Fe(n\text{-BuCp})(Cp)$	$\log_{10} p(\text{Torr}) = 34.32 - \frac{32840.4}{T(\text{K})+582.493}$		
$Bi(mmp)_3$	$\log_{10} p(\text{Torr}) = 8.2509 - \frac{2257.2}{T(\text{K})}$	293–343	[60]
$Bi(thd)_3$	$\log_{10} p(\text{Torr}) = 10.275 - \frac{5203}{T(\text{K})}$	293–343	[60]
$Fe(thd)_3$	$\log_{10} p(\text{Torr}) = 15.127 - \frac{6541}{T(\text{K})}$	359.8–377.8	[61]
$Fe(acac)_3$	$\log_{10} p(\text{Torr}) = 14.627 - \frac{6510.64}{T(\text{K})}$	369.3–387.5	[61]
$Y(thd)_3$	$\log_{10} p(\text{Torr}) = 16.617 - \frac{7392.92}{T(\text{K})}$; solid	395–435	[62]
	$\log_{10} p(\text{Torr}) = 10.475 - \frac{4674}{T(\text{K})}$; liquid	449–456	
$Ho(thd)_3$	$\log_{10} p(\text{Torr}) = 15.246 - \frac{6861.7}{T(\text{K})}$; solid	420–458	[43]
	$\log_{10} p(\text{Torr}) = 9.916 - \frac{4419.7}{T(\text{K})}$; liquid	458–500	
$Pr(thd)_3$	$\log_{10} p(\text{Torr}) = 18.033 - \frac{8637.2}{T(\text{K})}$; solid	450–495	[43]
	$\log_{10} p(\text{Torr}) = 12.109 - \frac{5703.7}{T(\text{K})}$; liquid	495–530	
$Tb(thd)_3$	$\log_{10} p(\text{Torr}) = 16.415 - \frac{7388.6}{T(\text{K})}$; solid	420–454	[43]
	$\log_{10} p(\text{Torr}) = 10.145 - \frac{4544.8}{T(\text{K})}$; liquid	454–500	
$Dy(thd)_3$	$\log_{10} p(\text{Torr}) = 15.484 - \frac{6972.1}{T(\text{K})}$; solid	410–456	[43]
	$\log_{10} p(\text{Torr}) = 10.067 - \frac{4504.6}{T(\text{K})}$; liquid	456–500	
$Er(thd)_3$	$\log_{10} p(\text{Torr}) = 15.526 - \frac{6955.5}{T(\text{K})}$; solid	410–454	[43]
	$\log_{10} p(\text{Torr}) = 10.065 - \frac{4478.3}{T(\text{K})}$; liquid	454–490	
$Ca(thd)_2$	$\log_{10} p(\text{Torr}) = 7.06 - \frac{3760}{T(\text{K})}$	383–553	[63]

analysis showed that the first mass loss temperature range was associated with partial dissociation or decomposition of the thd ligand. From the differential scanning calorimetry the second mass loss temperature range seemingly corresponds to clean evaporation of the precursor. However, the possibility that a small fraction of the precursor decomposes during evaporation via mechanisms observed for the first mass loss range could not be ruled out. $Bi(dmamp)(Me)_2$ is a liquid precursor with a vapor pressure of 0.1 Torr at 55 °C [66]. It evaporates in a single step at ~200 °C and starts to decompose at 230 °C. Its higher volatility in comparison with $Bi(Ph)_3$ has been attributed to its lower molecular mass. $Bi(mmp)_3$ is a highly air-sensitive solid alkoxide complex. The reported TG analysis shows a multi-step mass loss profile during evaporation which occurs in the temperature range 50–300 °C [67]. A large amount of non-volatile residue (40 %) was also observed and was attributed to the formation of hydrolyzed product that was reportedly difficult to avoid in case of the small sample size that was used in the TG analysis.

The TG analysis of $Fe(Cp)_2$ carried out in the temperature range 25–800 °C shows that it undergoes clean single step sublimation process in the range 50–200 °C resulting in almost 0% residue [68]. The thermal decomposition behavior of $(C_4H_9C_5H_4)Fe(Cp)$ is very similar to that of ferrocene. It evaporates in a single step in the range 50–240 °C, leaving behind only 2% residue [69]. This indicates a clean evaporation without any decomposition. $Fe(thd)_3$ is reported to melt in the range 160–182 °C and evaporate in the range 184–280 °C leaving a residue of about 1% [70]. Differential thermal analysis did not indicate any decomposition during evaporation. $Fe(acac)_3$ has been reported to evaporate in a single step in the range 150–230 °C and leaves a 6% residue [71].

$Y(thd)_3$ sublimes completely in the range 100–180 °C in a single step with no residue [72]. Mass spectrometry indicated that there was no degradation of precursor during evaporation. The atmospheric pressure TG curve of $Pr(thd)_3$ indicates that this precursor complex sublimes in a single step, in the 150–300 °C temperature range, with a 3–4% residue at 450 °C indicating clean vaporization with low residue [73]. $Tb(thd)_3$ sublimes in the range 150–260 °C and leaves a 3.3% residue [74]. Only one peak that corresponded to sublimation was observed in the differential scanning calorimetry data indicating that there was no decomposition during the sublimation process. $Er(thd)_3$ evaporates in the temperature range 100–190 °C and leaves no residue [75]. In case of $Ca(thd)_2$, a two-step mass loss due to evaporation of volatile impurities and vaporization of precursor has been reported [63]. No residue was left after the evaporation of $Ca(thd)_2$ complex. From the thermogravimetric analysis of $Mn(thd)_3$, it has been observed that it is thermally stable and vaporizes in a single step in the range 130–240 °C with a final residue of about 3% left at 300 °C [65]. The trivalent rare-earth ions have a tendency to attain a high coordination which results in polymerization. This tendency is stronger for the lighter lanthanides due to their larger ionic radius [42]. $Tb(thd)_3$ and $Dy(thd)_3$ are reported to undergo irreversible change from a dimeric form to monomeric form upon heating at 147 °C and 115 °C, respectively [76].

Although chemical solution deposition is a solution-based and less complex synthesis technique, the requirements for the precursors are challenging to meet. In order to successfully utilize the CSD technique, the precursors should meet a number of requirements as have been listed by Schwartz et al. [77]:

(i) the precursors should have sufficient solubility in the solvent,
(ii) the precursors should decompose without undesirable residues,

(iii) precursor components should not undergo phase separation during processing, and
(iv) precursor solution should be stable for obtaining desired films reproducibly.

The first two requirements are particularly restrictive and make metalorganics more suitable because their solubility can be tuned by choosing appropriate ligands and optimally tuned ligands would pyrolyze in an oxidizing atmosphere without leaving any residue. Precursors belonging to carboxylates, alkoxides and β-diketonates classes of metalorganics have been typically used in chemical solution deposition. These three classes differ in reactivity and solubility and result in different solution chemistries. Differences in precursor structures and solvent can exhibit significant effects in the properties of the deposited films. The sol–gel processes utilize alkoxides as starting reagents and alcohols such as 2-methoxyethanol as reactant and solvent. The key reactions in this synthesis route are hydrolysis, alcohol exchange and condensation of alkoxides. 2-Methoxyethanol has been the most widely used solvent due to its ability to dissolve a variety of metalorganics. The chelate processes also employ alkoxides but are based on a different key reaction which is the chelation of metal alkoxides by chelating agents such as acetic acid and acetylacetone. Chelation allows easy handling of the precursor solutions in air by lowering the hydrolysis tendency of alkoxides. However, the reaction chemistry in chelate process is quite complex making it hard to control the properties of the precursor solution. Metalorganic decomposition route involves dissolution of metal carboxylates in a common solvent such as xylene and combining these solutions to obtain desired stoichiometry in the films. This synthesis route is straightforward but suffers from limitations such as large shrinkage and mass loss due to the large organic ligands and limited process flexibility due to the minimal reactivity of the starting reagents. Details of the chemical solution deposition processes and precursor chemistries could be found in Refs. [78,79]. Table 3 lists the metalorganic precursors that have been reported for chemical solution deposition of $BiFeO_3$ and other multiferroics.

3. Routes for synthesis of multiferroic nanostructures from metalorganics

3.1. Metalorganic chemical vapor deposition

Chemical vapor deposition (CVD) refers to the process of depositing thin films of materials through a chemical reaction from the precursors present in the vapor phase. The process has been used to deposit thin films of a wide variety of materials for broad sets of applications. It is one of the most flexible and versatile yet a simple and robust process that can deposit conformal films with high purity and abrupt interfaces. It can deposit materials over a large area with high uniformity and high growth rates. It can work in different operating pressure regimes. It offers economical manufacturing making it highly suitable and preferred method of growing various kinds of materials in the industry. In situ thin film probing capabilities offer another advantage for research purposes.

When metalorganic compounds are used as precursors, the process is generally referred to as MOCVD. Depending upon the phase and properties of the precursors, various methods have been reported for delivery of precursor into the reactor. As mentioned in the previous section, the precursors for MOCVD should have certain properties. While precursors with inorganic ligands such as halides may be suitable, those are beyond the scope of this paper. Depending upon the processing conditions, reactor configuration, precursor delivery method and whether external agent is used to induce the reaction, different MOCVD variants are available, for example, low-pressure MOCVD, atmospheric pressure MOCVD, hot-wall/cold-wall MOCVD, horizontal/vertical MOCVD, direct-liquid injection (DLI) MOCVD, and plasma-enhanced (PE) MOCVD.

Since the available metalorganic sources for multiferroic materials are mostly solids, there are a few major precursor delivery methods worth mentioning. These methods mainly differ in whether the phase of the precursor when delivered to the reactor is solid or liquid. One approach has been the liquid injection wherein the precursor is dissolved in an appropriate solvent and then injected in a controlled manner into a heated unit where it gets flash vaporized and the vapors are then flowed into the reactor with or without the use of a carrier gas. In the case when multiple precursors are to be used, precursors may be injected independently from independent solutions [47] or they could alternatively be injected in the form of a solution prepared by carefully mixing the different precursors in the same solvent [102]. The use of a solvent raises the possibility of organic contamination in the films. Also, particularly in the case of mixed precursors, appropriate solvent needs to be determined using solubility and viscosity tests [48]. In a band-flash type of setup, the choice of solvent becomes more relaxed [102,103] (Fig. 7).

Alternatively, instead of using a solvent-based approach, one can also use solid precursors directly by employing various means. In one approach, one may provide a separate heating zone where a crucible containing the precursor may be kept and then using a carrier gas the vapors can be flown into the reaction zone. This method though simple, does not provide any control of the amount of precursor flowing to the substrate. Another approach is to mix the precursors in appropriate quantities together in the powder form and make a disk by compaction. Then microportions from this disk may be sliced and fed to the reactor [104] (Fig. 8).

3.1.1. Single-phase multiferroic materials

3.1.1.1. $BiFeO_3$. Ueno et al deposited epitaxial $BiFeO_3$ films using $Bi((CH_3)_2(2\text{-}(CH_3)_2NCH_2C_6H_4))$ and $Fe(C_2H_5C_5H_4)_2$ as precursors in a bubbler-type delivery MOCVD setup [45]. The Bi:Fe molar ratio in the films correlated with the molar ratio of precursors in the feed gas. The films were deposited on $SrRuO_3/SrTiO_3$ substrates at 620 °C. For 480 nm thick $BiFeO_3$ films, polarization hysteresis loops with remanent polarization 51 μC/cm^2 and coercive field 166 kV/cm were obtained at 80 K.

Yang et al. used liquid delivery MOCVD to grow epitaxial $BiFeO_3$ films on $SrRuO_3/SrTiO_3$ and $SrRuO_3/SrTiO_3$/Si substrates at 650 °C [46]. $Bi(thd)_3$ and $Fe(thd)_3$ dissolved in tetrahydrofuran were used as the source metalorganics. To avoid condensation of the vaporized precursors, a showerhead heated with oil was used. The Bi/(Bi + Fe) ratio in the precursor solution was varied between 0.5 and 0.85 in order to optimize the film composition. Bi/(Bi + Fe) ratio of 0.7 was optimal to obtain stoichiometric $BiFeO_3$ films. Smaller polarization values and coercive field values were observed for films deposited

Table 3
Combinations of precursors reported for CSD of single-phase multiferroic materials.

Deposited material	Precursors	Reference
$BiFeO_3$	$Bi(CH_3COO)_3$; $Fe(acac)_3$	[32,80–88]
	$Bi(O^tC_5H_{11})_3$; $Fe(OC_2H_5)_3$	[89]
	$Bi(O^nC_4H_9)_3$; $Fe(acac)_3$	[90]
	$Bi(O^tC_4H_9)_3$; $Fe(O^tC_4H_9)_3$	[91]
	$Bi(O^tC_5H_{11})_3$; $Fe(acac)_3$	[30,92]
	$Bi(OCO(CH)(C_2H_5)(C_4H_9)_3$; $Fe(acac)_3$	[93]
$YMnO_3$	$Y(CH_3CO_2)_3{\cdot}4H_2O$; $Mn(CH_3CO_2)_2{\cdot}4H_2O$	[94–96]
	$Y(O^iPr)_3$; $Mn(CH_3CO_2)_2{\cdot}4H_2O$	[97–99]
	$Y(O^iPr)_3$; $Mn(O^iPr)_2$	[100]
	$[Y(OC_2H_4OCH_3)_3]_{10}$; $Mn(OC_2H_4OCH_3)_2$	[101]

acac: acetylacetonate.

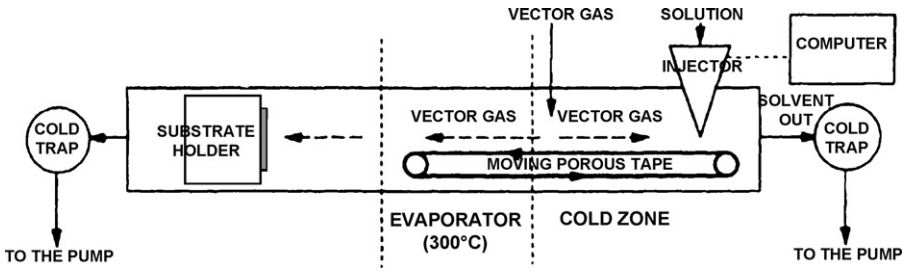

Fig. 7. The droplets are injected on the moving tape, the solvent evaporates in the cold zone and is eliminated at right end. The tape carries the dry precursor toward the evaporator, where the vector gas flowing to the left part carries the precursor vapors toward the substrate.
Figure was reproduced from Ref. [102], with permission of the copyright holders.

on $SrRuO_3/SrTiO_3/Si$ compared to those for the films deposited on $SrRuO_3/SrTiO_3$.

Tasaki et al. compared various precursors for liquid delivery MOCVD of $BiFeO_3$ films [47]. Bismuth aryls—Bi(*o*-Tol)$_3$ and Bi(*p*-Tol)$_3$—were studied as bismuth sources, while iron β-diketonates (Fe(DPM)$_3$, Fe(TMOD)$_3$, Fe(DIBM)$_3$ and Fe(IBPM)$_3$) and iron cyclopentadienyls (Fe(Cp)$_2$ and Fe(MeCp)$_2$) were compared as the iron sources. Bismuth and iron precursors were dissolved in toluene in order to prepare the precursor solution for use in the liquid delivery MOCVD apparatus. Bi(*p*-Tol)$_3$ was reported to be a better bismuth precursor since the bismuth content in the films was more controllable in case of Bi(*p*-Tol)$_3$ compared to Bi(*o*-Tol)$_3$. Bi(*p*-Tol)$_3$ was selected as the bismuth precursor for comparative studies on the iron precursors. Fe content in the films was very low in case of cyclopentadienyls compared to β-diketonates. For depositing stoichiometric $BiFeO_3$ films, Bi(*p*-Tol)$_3$ and Fe(DIBM)$_3$ mixed in ratio 2:1 were chosen as precursors. X-ray diffraction (XRD) analyses showed that the films deposited at 500 °C and 525 °C were $BiFeO_3$ while films deposited 550 °C also had Bi_2O_3 phase present. The films deposited at 525 °C were reported to be ferroelectric though the observed remanent polarization (less than 2 $\mu C/cm^2$) was very low.

Thery et al. compared two different bismuth precursors—Bi(thd)$_3$ and Bi(mmp)$_3$—for depositing $BiFeO_3$ films while Fe(thd)$_3$ was fixed as the Fe source [48]. Various commonly used solvents were compared for preparing the precursor solution. Bi(mmp)$_3$ was reported to be more suitable Bi source. The $BiFeO_3$ films were deposited at 550 °C and 666 Pa (5 Torr) on $SrTiO_3$ substrates in a pulsed liquid delivery MOCVD. XRD and TEM analyses did not reveal any secondary phases. However, XPS indicated presence of Fe in mixed valence states which apparently led to the magnetization value (70 emu cm^{-3}) which is much higher than the bulk value for $BiFeO_3$.

Kartavtseva et al. reported growth of epitaxial $BiFeO_3$ films on (0 0 1) $SrTiO_3$ using single-source MOCVD [49]. Bi(Ph)$_3$ and Fe(thd)$_3$ were used as the precursors for growing the films in the temperature range 500–800 °C and a total pressure 1.2–1.8 kPa. The saturation magnetization for the film was measured to be 9 kA/m (9 emu cm^{-3}).

Singh et al. prepared $BiFeO_3$ nanofilms on platinized silicon substrates [Pt(111)/TiO_2/SiO_2/Si] by MOCVD using *n*-butylferrocene and triphenylbismuth [50]. The films deposited at 550 °C and 15 Torr were polycrystalline and had a saturation magnetization of ~8 emu cm^{-3} at room temperature. Using electrostatic force microscopy, the films were observed to have ferroelectric characteristics. Magneto-dielectric coupling was observed through the measurements of magnetic field dependence of real and imaginary parts of the effective dielectric constant at 18 GHz. The coupling indicates the potential use of $BiFeO_3$ films in tunable high-frequency devices.

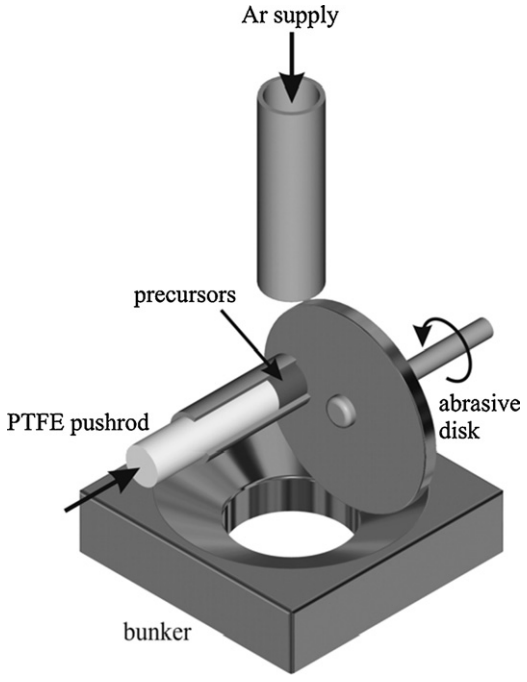

Fig. 8. Schematic of the shaving solid feeder.
Figure was reproduced from Ref. [104], with permission of the copyright holders.

3.1.1.2. $YMnO_3$. Choi et al. used MOCVD to deposit $YMnO_3$ films on Y_2O_3 buffered p-type Si(1 0 0) substrates at 500 °C and 3 Torr for FeRAM applications [51]. Metalorganics Y(thd)$_3$ and methylcyclopentadienylmanganese tricarbonyl ($(CH_3C_5H_4)Mn(CO)_3$) kept in individual bubblers were used as sources for Y and Mn, respectively. The Y(thd)$_3$ and $(CH_3C_5H_4)Mn(CO)_3$ bubblers were kept at 162 °C and 20 °C, respectively. The deposited films annealed for 60 min in 100 mTorr vacuum at 750 °C were observed to have superior properties (crystallinity, ferroelectricity and low leakage) compared to films annealed in oxygen. Magnetic behavior was not reported for these films.

Bosak et al. deposited single-phase epitaxial $YMnO_3$ films on $LaAlO_3$ (0 0 1) and $SrTiO_3$ (0 0 1) substrates using Y(thd)$_3$ and Mn(thd)$_3$ [52]. The MOCVD used a single-source band-flash evaporation method for precursor delivery [103]. The films were grown at 840 °C and 1300 Pa (9.75 Torr) with oxygen partial pressure of 435 Pa (3.26 Torr). Epitaxial stabilization due to low lattice mismatch substrates enabled the growth of the films in the perovskite structure instead of the stable hexagonal form. Interestingly, it is the hexagonal phase that exhibits multiferroicity.

More recently, Kim et al. used metalorganics Y(thd)$_3$ and Mn(thd)$_3$ in a liquid precursor injection MOCVD reactor to deposit $YMnO_3$ films on Pt/Ti/SiO_2/Si substrates at 10 Torr and 450–600 °C [53]. A flash evaporator maintained below 300 °C was used to vaporize the precursor solution (0.03 M Y(thd)$_3$ and Mn(thd)$_3$ in tetrahydrofuran). Films annealed at 830 °C in inert ambient were

observed to crystallize in hexagonal $YMnO_3$ phase. Ferroelectric loop measurements revealed a remanent polarization of 2 $\mu C/cm^2$ and coercive field of 10 kV/cm. Magnetization behavior was not reported for these films.

Dubourdieu et al. synthesized thin films of hexagonal $YMnO_3$ by liquid delivery MOCVD using $Y(thd)_3$ and $Mn(thd)_3$ metalorganic precursors [33]. The precursors mixed in monoglyme solvent were injected into an evaporator held at 250 °C. Films were grown on (1 1 1) $ZrO_2(Y_2O_3)$ and Pt(1 1 1)/TiO_2/SiO_2/Si substrates at 800–900 °C and total pressure of 660 Pa (5 Torr) with oxygen partial pressure of 0.33 kPa (2.5 Torr). In situ annealing of the samples in 100 kPa (750 Torr) O_2 was done after deposition. Though, mainly, *c*-axis oriented films were obtained on both the substrates, films deposited on platinized silicon had larger amount of secondary orientations and also had some perovskite phase present. From the neutron diffraction experiments at different temperatures, T_N was estimated to be 66 K [55].

3.1.1.3. $HoMnO_3$. Bosak et al. deposited single-phase epitaxial $HoMnO_3$ films on $LaAlO_3$ (0 0 1) and $SrTiO_3$ (0 0 1) substrates using $Ho(thd)_3$ and $Mn(thd)_3$ [52]. The MOCVD used a single-source band-flash evaporation method for precursor delivery [103]. The films were grown at 840 °C and 1300 Pa (9.75 Torr) with oxygen partial pressure of 435 Pa (3.26 Torr). Epitaxial stabilization due to low lattice mismatch substrates enabled the growth of the films in the perovskite structure instead of the stable hexagonal form.

Dubourdieu et al. synthesized thin films of hexagonal $HoMnO_3$ by liquid delivery MOCVD using $Ho(thd)_3$ and $Mn(thd)_3$ metalorganic precursors [33]. The precursors mixed in monoglyme solvent were injected into an evaporator held at 250 °C. Films were grown on (1 1 1) $ZrO_2(Y_2O_3)$ and Pt(1 1 1)/TiO_2/SiO_2/Si substrates at 800–900 °C and total pressure of 660 Pa (5 Torr) with oxygen partial pressure of 0.33 kPa (2.5 Torr). In situ annealing of the samples in 100 kPa (750 Torr) O_2 was done after deposition. The films had *c*-axis oriented perpendicular to the substrate. For films thicker than 100 nm secondary orientations were also observed. In the neutron diffraction analysis, T_N was not clearly observed though a magnetic transition at 50 K corresponding to reorientation temperature on bulk $HoMnO_3$ was observed [55].

3.1.1.4. $DyMnO_3$. Bosak et al. deposited single-phase epitaxial $DyMnO_3$ films on $LaAlO_3$ (0 0 1) and $SrTiO_3$ (0 0 1) substrates using $Dy(thd)_3$ and $Mn(thd)_3$ [52]. The MOCVD used a single-source band-flash evaporation method for precursor delivery [103]. The films were grown at 840 °C and 1300 Pa (9.75 Torr) with oxygen partial pressure of 435 Pa (3.26 Torr). The films had perovskite structure instead of desired hexagonal structure. In a later report, Bosak et al. used (1 1 1) $ZrO_2(Y_2O_3)$ substrate to induce epitaxial stabilization to obtain the hexagonal structure [54]. The films were synthesized by liquid injection MOCVD at 900 °C and 670 Pa using the same precursors as before.

Dubourdieu et al. synthesized thin films of hexagonal $DyMnO_3$ by liquid delivery MOCVD using $Dy(thd)_3$ and $Mn(thd)_3$ metalorganic precursors [33]. The precursors mixed in monoglyme solvent were injected into an evaporator held at 250 °C. Films were grown on (1 1 1) $ZrO_2(Y_2O_3)$ and Pt(1 1 1)/TiO_2/SiO_2/Si substrates at 800–900 °C and total pressure of 660 Pa (5 Torr) with oxygen partial pressure of 0.33 kPa (2.5 Torr). In situ annealing of the samples in 100 kPa (750 Torr) O_2 was done after deposition. Though the stable phase for $DyMnO_3$ is the perovskite structure, the metastable hexagonal phase was obtained because of epitaxial stabilization.

3.1.1.5. $TbMnO_3$. Dubourdieu et al. synthesized thin films of hexagonal $TbMnO_3$ by liquid delivery MOCVD using $Tb(thd)_3$ and $Mn(thd)_3$ metalorganic precursors [33]. The precursors mixed in monoglyme solvent were injected into an evaporator held at 250 °C. Films were grown on (1 1 1) $ZrO_2(Y_2O_3)$ substrates at 800–900 °C and total pressure of 660 Pa (5 Torr) with oxygen partial pressure of 0.33 kPa (2.5 Torr). In situ annealing of the samples in 100 kPa (750 Torr) O_2 was done after deposition. Epitaxial stabilization enabled the deposition of the hexagonal phase of $TbMnO_3$.

3.1.1.6. $ErMnO_3$. Thin $ErMnO_3$ films (450–500 nm) were deposited on (1 1 1) $ZrO_2(Y_2O_3)$ substrates by liquid injection MOCVD using $Er(thd)_3$ and $Mn(thd)_3$ as precursors. T_N ~68 K was estimated from the neutron diffraction experiments for 500 nm thick films [55].

3.1.1.7. $Pr_{(1-x)}Ca_xMnO_3$. Nakamura et al. used a liquid injection MOCVD to deposit 300 nm $Pr_{(1-x)}Ca_xMnO_3$ films on Pt/SiO_2/Si substrates at 480 °C and 5 Torr [105]. $Pr(thd)_3$, $Ca(thd)_2$ and $Mn(thd)_3$ dissolved in tetrahydrofuran were used as the precursors. Each dissolved precursor was carried by N_2 into a vaporizer and then the reactor where O_2 was mixed in. After deposition the films were annealed at 600 °C for 5 h. The films showed reversible resistance switching upon application of electrical pulses [106].

3.1.2. Multiferroic structures

Work on preparation of doped-multiferroics or composites using MOCVD is non-existent, though reports on MOCVD of ferrites alone exist. Only acetylacetonate complexes have been used as precursors in these reports.

Itoh et al. prepared (Ni, Zn)Fe_2O_4 films on silica glass and MgO (1 0 0) substrates in a low-pressure MOCVD using thermal decomposition of acetylacetonate complexes [107]. The solid precursors $Ni(acac)_2$, $Zn(acac)_2$ and $Fe(acac)_2$ were evaporated by heating in independent furnaces at 157 °C, 79 °C and 146 °C, respectively, and were carried by N_2 to the reactor. Oxygen was used as the oxidizer and the depositions were done at 12 Torr in temperature range 400–800 °C. The $NiFe_2O_4$ films deposited on silica glass between 400 and 450 °C had low crystallinity. The saturation magnetization and crystallinity increased with deposition temperature. Films deposited above 600 °C were epitaxial and had a saturation magnetization of 40–50 emu g^{-1}. (Ni,Zn)Fe_2O_4 films deposited on silica glass between 500 and 600 °C were polycrystalline with saturation magnetization 54–62 emu g^{-1} and coercive force 50–100 Oe. In comparison, films grown on MgO between 600 and 650 °C were epitaxial and showed higher saturation magnetization (60–67 emu g^{-1}) and lower coercive force (20–30 Oe).

Fujii et al. synthesized thin films of $CoFe_2O_4$ and $Co_{(1-x)}Zn_xFe_2O_4$ ($0 \le x \le 0.5$) by plasma-enhanced MOCVD using metal acetylacetonate complexes [108] at a lower temperature. The soda-lime glass substrate was kept at 400 °C and the depositions were done at 10 Pa with a 400 W rf power. $Fe(acac)_3$, $Co(acac)_3$ and $Zn(acac)_2$ vaporized at 135 °C, 145–152 °C and 66–76 °C, respectively, were used as the metal sources. The deposited Co–Zn ferrite films had a (1 0 0) texture with a columnar structure. Faraday hysteresis loops indicated that the films had perpendicular magnetic anisotropy with a coercive force of 3200 Oe. The Faraday rotation at 800 nm and the Curie temperature were observed to decrease with increasing Zn content; this was attributed to the substitution of Co^{2+} in tetrahedral sites of $CoFe_2O_4$ by non-magnetic Zn^{2+}.

Langlet et al. deposited (Ni,Zn) ferrite thin films by a CVD process in which an aerosol of precursor was transported into the reactor and then pyrolyzed on glass substrate at 460 °C [109]. A solution of metal acetylacetonate precursors dissolved in butanol was kept in a glass container fitted with a piezoelectric transducer which was excited to generate aerosol. The films were annealed at 500 °C in air to improve crystallization. The films were polycrystalline and had cubic spinel phase. The metal concentration ratio in the films was different from that in the precursor solution; this was attributed to differences in the thermal stability of the metal acetylacetonates

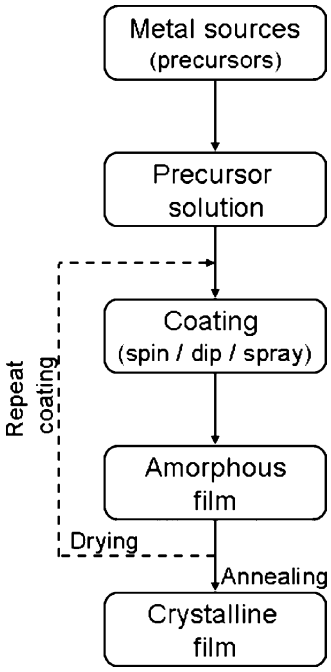

Fig. 9. Different steps in a typical chemical solution deposition process.

used. The saturation magnetization ranged from 70–280 emu cm^{-3} depending upon the composition of the ferrite.

3.2. Chemical solution deposition

The CSD method is another versatile technique for synthesizing thin films. This method refers to approaches such as sol–gel and metalorganic decomposition which have been recently used for depositing various kinds of high-quality thin film materials including oxides. Fig. 9 illustrates the general steps involved in a CSD process. Suitable precursors, such as inorganic salts and metalorganics, are chosen and dissolved in a solvent. The precursor solutions are then mixed together in ratios chosen so as to yield desired stoichiometry in the deposited films. This mixed solution is then used to coat the flat substrates by spin-, spray- or dip-coating process. The films are then dried to remove organic material and the coating process is repeated if the desired thickness is not achieved with a single coating step. The film is finally subjected to annealing in air or oxygen to improve the crystallinity and microstructure. The CSD technique with details of the processing steps and the underlying thermodynamics has been reviewed in Refs. [77,110,111]. In this review, the focus is on CSD using metalorganic precursors such as acetates, carboxylates, alkoxides and β-diketonates. It is important to note that chemical vapor deposition results in continuous growth, whereas in the case of CSD a thickness of 20–100 nm is typically crystallized at the same time. Also, since only the top surface of film is in contact with the ambient, it is hard to control the partial pressure of oxygen in the bulk of the film [112].

3.2.1. Single-phase multiferroic materials

3.2.1.1. $BiFeO_3$. Bismuth acetate and iron acetylacetonate has been the most popular combination for chemical solution deposition of $BiFeO_3$ films [80,82–84,86,88]. Qi et al. used bismuth acetate and iron acetylacetonate dissolved in acetic acid and acetone to deposit $BiFeO_3$ films on $SrTiO_3$ and $LaAlO_3$ substrates by sol–gel technique [86,113]. For thicknesses less than 300 nm, highly *c*-axis oriented $BiFeO_3$ films were obtained. The final composition and surface morphology of the films was reported to be sensitive to the sintering process. The films sintered at 780 °C showed high porosity and presence of $Bi_2Fe_4O_9$ impurity phase. This was attributed to the volatility of Bi. The films were reported to be antiferromagnetic or paramagnetic since the magnetization showed a small linear increase with applied magnetic field. The ferroelectric characteristics were not investigated.

Chung and Wu used propionic acid as the solvent for these precursors to deposit $BiFeO_3$ films [83]. They studied the effect of annealing temperature on the current leakage, dielectric constant and polarization of the films. For the films annealed between 350 and 550 °C, the grains were uniform and increased slightly from 30 nm at 350 °C to 50 nm at 550 °C. However, the films annealed at 600 °C had large grains (~1000 nm) as well as small grains (70–100 nm). No secondary phases were reported to be observed for all these annealed films. The leakage current for the annealed films at 10 kV/cm was less than 10^{-7} A/cm^2 and decreased with increasing annealing temperature up to 550 °C above which it increased. The trend in leakage currents with increasing annealing temperatures was attributed to changes in grain size. The remanent polarization of the films did not vary much with annealing temperatures and was 30 μC/cm^2. The coercive field for films annealed above 450 °C was close to 80 kV/cm. Iakovlev et al. reported fabrication of $BiFeO_3$ polycrystalline films by CSD using these precursors in acetic acid and DI water [80]. A 0.25 mol/l solution was prepared by dissolving the precursors in DI water and acetic acid mixed in 1:2 volume ratio. The prepared solution had 2 mol% excess Bi in order to compensate for loss during annealing. Thin films were prepared by successive spin-coating (5000 rpm, 30 s) this solution on (1 1 1) Pt/Ti/SiO_2/Si substrates. After each coating, the deposited layer was dried on a hot plate. The films were annealed in oxygen/air at 650 °C for 1 h. The films were crack-free and had a partial (1 0 0) texture. Films annealed in oxygen have a more dense structure with finer crystallites and had higher electrical resistance. The oxygen annealed films exhibited poor ferroelectric behavior ($2P_r$ ~1 μC/cm^2) and had a 12 pm/V piezoelectric coefficient which was independent of the applied voltage amplitude.

Habouti et al. reported substantial improvement in leakage resistance for their sol–gel $BiFeO_3$ films deposited with assistance of UV pyrolysis (UVP) [84]. Compared to the $BiFeO_3$ films deposited with no UV pyrolysis (NP), the UVP films had better crystallinity as inferred from the stronger intensities of the peaks in diffractogram. The films had strong (1 0 0) preferred orientation. Also, SEM micrographs indicated a fine-grained smooth topography for UVP films in contrast to the rougher grain morphology as observed for NP films. It was speculated that UV treatment caused early cracking of C–H bonds and formation of highly activated oxygen species that led to efficient pyrolysis resulting in the observed fine morphology. The UVP films had leakage currents several orders of magnitude less than those observed in NP films. However, the ferroelectric polarization remained poor for the films. The saturation magnetization of the UVP and NP films was 55.4 emu cm^{-3} and 45.8 emu cm^{-3}, respectively.

Tyholdt et al. synthesized $BiFeO_3$ films by spin-coating a sol prepared by alcoholysis of $Fe(O^tBu)_3$ and $Bi(O^tBu)_3$ in 2-methoxyethanol [91]. Using sols with 0% and 10% Bi excess, films were deposited on Pt/TiO_2/SiO_2/Si(1 0 0) substrates. The films were crystallized at 500, 600 or 700 °C for 20 min. Phase pure (0 1 2)-oriented films were obtained with the preferred texture being more enhanced in films prepared using 10% Bi excess sol. The texture increased with increasing crystallization temperature. The films deposited with 10% Bi excess were smoother and had a denser microstructure. Surface analysis indicated the presence of some excess Bi at the film surface.

Nakamura et al. used a solution of 2-ethylhexanoate bismuth [$Bi(OCO(CH)(C_2H_5)C_4H_9)_3$] and $Fe(acac)_3$ to spin coat 250 nm thick $BiFeO_3$ films on Pt/TiO_2/SiO_2/Si substrates [93]. Two solutions with

0% and 10% excess Bi were used to prepare three different structures of stoichiometric $BiFeO_3$ thin film with (i) Bi excess top layer (Bi–T), (ii) bottom layer (Bi–B), and (iii) top and bottom layer (Bi–TB). The films were polycrystalline with Bi–TB and Bi–B structures having the best and worst crystallinity, respectively. It was speculated the Bi excess layers at the top and bottom could accelerate the crystallization. The films on Bi–TB had larger grain size compared to the other two structures and had the best ferroelectric property (P_r = 55 μC/cm^2 and coercive field of 385 kV/cm at room temperature). The saturation magnetization at 80 K was 16 emu cm^{-3} attributed to the suppression of inhomogeneous cycloidal magnetic spin structure [114]. In another related study, they investigated $BiFeO_3$ films with different Bi/Fe ratios [115]. $BiFeO_3$ films with 10% Fe excess, and 5%, 10% and 20% Bi excess were deposited using the same precursors and procedures as in Ref. [93]. All deposited films were mainly polycrystalline perovskite. However, 10% Fe excess films had $Bi_2Fe_4O_9$ while 20% Bi excess films had Bi_2O_3 present as impurity phase. AFM analyses revealed that all films had a rosette structure consisting of circular regions with an uneven texture surrounded by regions with flat surface. The roughness of these circular regions increased with increasing Bi/Fe ratio. Further probing with Raman spectroscopy revealed that the circular regions were crystalline $BiFeO_3$ while the outer regions were amorphous $BiFeO_3$. The films with excess Bi showed larger leakage currents. The remanent polarizations for a maximum applied electric field of 1.2 MV/cm were 30, 38, 28, 85 and 53 μC/cm^2 for the 10% Fe excess, stoichiometric, 5% Bi excess, 10% Bi excess and 20 % Bi excess films, respectively.

3.2.1.2. $YMnO_3$. Teowee et al. synthesized $YMnO_3$ films via sol–gel process from a 0.25 M yttrium manganate solution prepared using yttrium acetate, manganese acetate and methanol [94]. The solution was spin-coated at 2000 rpm for 30 s on platinized silicon wafers and then fired in oxygen at 400 °C between successive coatings. The deposited films were annealed at different temperatures. Films annealed up to 750 °C were amorphous and those annealed above 800 °C were fully crystallized in hexagonal phase. However, the polarization hysteresis loops indicated the films had low polarization (0.5 μC/cm^2 at 228 K) and high charge leakage behavior.

Tadanaga et al. prepared 300 nm $YMnO_3$ thin films on Pt, Si(1 1 1) and Pt/Ti/SiO_2/Si(1 0 0) substrates by sol–gel method via two different routes—thermal decomposition and reflux—using $Y(OAc)_3{\cdot}4H_2O$ and $Mn(OAc)_2{\cdot}4H_2O$ as precursors [116]. For thermal decomposition route, a solution was prepared by mixing the precursors individually dissolved in ethanol containing diethanolamine (DEA), whereas 2-ethoxyethanol was used for the reflux process. In case of thermal decomposition, single-phase hexagonal $YMnO_3$ films were obtained after annealing at 900 °C, while in the case of reflux process, hexagonal films were obtained above 800 °C. However, stoichiometric $YMnO_3$ films had large dielectric losses due to pinholes, and 5–10% excess Y improved the properties. Later, they studied the effect of addition of DEA in the manganese precursor solution for deposition of $YMnO_3$ films [95]. Manganese precursor solution was prepared by dissolving $Mn(OAc)_2{\cdot}4H_2O$ in 2-ethoxyethanol with or without the addition of DEA. The solution was dehydrated and refluxed at 125 °C for 3 h. Yttrium precursor solution was prepared similarly but with addition of DEA. The two precursor solutions were then mixed together and refluxed for 5 h at 125 °C. This solution was then used to coat Pt, quartz glass and Pt/sapphire substrates using a dipping method. The deposited films were then thermally treated in air at 400 °C for 15 min to remove the residual organics. These coating and thermal treatment steps were repeated several times to obtain desired film thickness. The final structure was then annealed in air at 800–900 °C for 2–3 h. It was observed that the films deposited from the solution with addition of DEA to the Mn precursor had *c*-axis preferred orientation whereas the films deposited from solution without the addition of DEA had random orientations. It was also reported that the films heat treated in vacuum had very low leakage current and ferroelectricity could be observed even at room temperature. In another work, they reported a lowering in the crystallization temperature to 500 °C when yttrium tri-isopropoxide was used as the yttrium precursor [97]. The permittivity measured at 100 kHz for the films heat treated at 500, 600 and 700 °C was 40, 50 and 70, respectively, while the dissipation factor was 0.10, 0.10 and 0.25, respectively. However, the films had a relatively large leakage current (~2.4×10^{-4} A/cm^2).

Kim and Kim studied the effect of drying temperature on the properties of $YMnO_3$ films deposited using sol–gel [96]. Yttrium acetate hydrate and manganese acetate hydrate were dissolved in 2-methoxyethanol separately and refluxed at 125 °C for 3 h. The solutions were then mixed to give an equimolar Y:Mn solution which was refluxed at 70 °C for 2 h and then distilled at 125 °C for 5 h. Distilled water and acetyl acetone were added to obtain a 0.15 M $YMnO_3$ which was further refluxed. $YMnO_3$ films were then deposited on (1 1 1) Pt/Ti/SiO_2/Si or Si substrate by spin-coating (4000 rpm, 30 s). Drying at various temperatures (300–450 °C) was done in between successive coatings. The coating/drying steps were repeated seven times to get 300 nm thick films. These films were finally annealed at 850 °C in O_2 for 1 h. For films dried at 450 °C, the peak intensity of (0 0 0 4) peak increased rapidly indicating stronger *c*-axis orientation of the films. The films dried below 400 °C showed no preferred orientation. With increasing drying temperature, the grain size and surface roughness also increased. Electrical measurements performed indicated that the films dried at higher temperature had a higher permittivity and lower leakage currents. The remanent polarization value was maximum for films dried at 450 °C ($2P_r$ ~3.6 μC/cm^2).

$YMnO_3$ films were prepared on Si substrates by chemical solution deposition using yttrium tri-iso-propoxide and manganese acetylacetonate dissolved in 2-methoxyethanol with small amounts of acetic acid [98] or acetylacetone [99]. The films prepared with acetic acid in precursor solution were finally annealed in air at 800 °C for 1 h. In case of films prepared with acetylacetone in solution, annealing was done in air at 650 °C for 40 s. The films had a (0 0 0 1) oriented hexagonal structure, however, ferroelectricity at room temperature could not be observed.

Suzuki et al. reported preparation of $YMnO_3$ films by chemical solution deposition using yttrium isopropoxide and manganese isopropoxide dissolved in ethylene glycol monomethyl ether [100]. The precursor solution was spin-coated on Pt(1 1 1)/TiO_x/SiO_2/Si substrates. The as-deposited films were dried at 150 °C, calcined at 350 °C and finally rapid thermal annealed at 750 °C in vacuum or oxygen ambience. The films annealed in vacuum had hexagonal structure with small grain size (30–50 nm) but low *c*-axis orientation. The films annealed in oxygen, on the other hand, were a mixture of hexagonal and perovskite phases with larger grain size (100–150 nm). Interestingly, a two-step annealing process where the films were first annealed in vacuum for 7 s followed by 10 min annealing in flowing oxygen, produced *c*-axis oriented hexagonal $YMnO_3$ films. The first step restrained the crystallization in the perovskite phase while the latter promoted the *c*-axis orientation. Films annealed in argon had remanent polarization of 2.1 μC/cm^2 and coercive field of 110 kV/cm [117].

Westin and Jansson prepared $YMnO_3$ films on platinized substrates by sol–gel using alkoxide precursors $[Y(OC_2H_4OCH_3)_3]_{10}$ and $Mn(OC_2H_4OCH_3)_2$ [101]. The films had hexagonal structure with minor amounts of orthorhombic phase. However, the study focused only on the deposition process and no electrical properties for the obtained films were reported.

3.2.2. Multiferroic structures

3.2.2.1. Doped materials. Chung et al. reported the electrical properties of Mn- and Nb-doped $BiFeO_3$ thin films (200 nm) deposited by CSD [81]. Bismuth acetate, iron acetylacetonate, manganese acetate and niobium ethoxide were used as the metal sources. Precursor solutions with different compositions were prepared using propionic acid as solvent and 2-methoxyethanol as additive. The dopants did not affect the crystal structure of $BiFeO_3$; the doped films were smooth, dense and polycrystalline having pure perovskite phase with decreased grain size. However, the effect on electric properties was significant. The doped films had higher permittivity values. The leakage behavior was also different from the pure $BiFeO_3$ films. Mn-doped films showed an Ohmic conduction behavior where the conductivity increased with increasing dopant concentration. Though, Mn ions were mainly present as Mn^{3+}, the presence of some Mn^{2+} was attributed for the increase in oxygen vacancies and, thereby, the increased leakage behavior of the Mn-doped films. In case of the Nb-doped films, grain boundary limited conduction behavior was observed. This was explained by the significant decrease in oxygen vacancies and grain size due to presence of Nb^{5+}. Nb-doped $BiFeO_3$ films also showed better ferroelectric behavior than the pure $BiFeO_3$ films (Fig. 10).

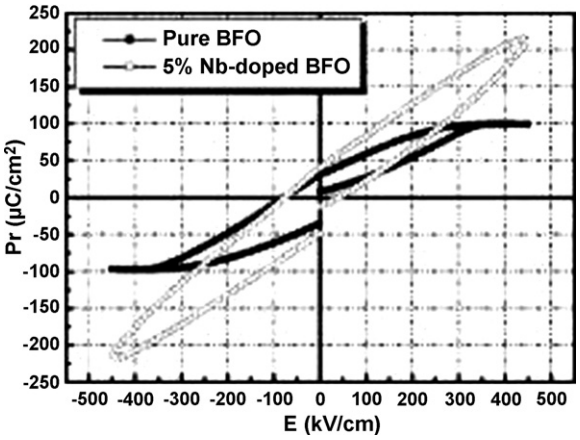

Fig. 10. Effect of Nb-doping in the $BiFeO_3$ films.
Figure was reproduced from Ref. [81], with permission of the copyright holders.

Brinkman et al. deposited 0%, 2%, 5% and 15% Sr-doped $BiFeO_3$ films (~1 μm thick) by chemical solution deposition using bismuth acetate, $Fe(acac)_3$ and $Sr(acac)_2$ dissolved in acetic acid and water [32]. The crystal structure as well as electrical properties was affected by addition of Sr dopants. The pure and 2% Sr-doped $BiFeO_3$ films had distinct (1 0 4) and (1 1 0) peaks, which merged into single broad peak upon further addition of Sr dopants (Fig. 11(a)) indicating a loss of anisotropy and reduction in grain size which were also evident in the SEM images (Fig. 11(b)). As expected of an acceptor dopant, the Sr-doped $BiFeO_3$ films showed increased leakage current densities.

Singh et al. deposited 0%, 5%, 10% and 20% La-doped $BiFeO_3$ films (400 nm) from a sol–gel prepared using $Bi(O^nC_4H_9)_3$, $Fe(acac)_3$ and $La(O^nC_4H_9)_3$ dissolved in 2-ethylhexanoic acid [90]. The films were annealed in a nitrogen atmosphere at 550 °C for 10 min. The films crystallized in single perovskite phase with mixed orientations. The grain size increased with La concentration while the leakage current decreased. P_r was 50 μC/cm² for 5% La-substituted BFO film. Uchida et al. fabricated La- and Nd-doped BFO films (300 nm) by CSD using $Bi(O^tC_5H_{11})_3$, $La(O^iC_3H_7)_3$, $Nd(O^iC_3H_7)_3$ and $Fe(acaca)_3$ [30]. Films with less than 5% doping had random orientations while the films with more than 10% doping were highly oriented. It was observed that the lattice spacing d_{101} and lattice parameter c decreased gradually with increasing dopant content indicating lowering of crystal anisotropy. Although, the electrical resistivity of the BFO films was improved upon doping with Nd^{3+}, the ferroelectric properties degraded as indicated by the non-saturated polarization loops. In case of La^{3+}-doped films, even the resistivity degraded. Additionally, current densities for the doped films measured at 10 K were observed to be much lower than the densities at room temperature indicating the presence of undesirable conduction paths even after doping with rare-earth ions. Habouti et al. [85] fabricated 0%, 5% and 10% $LaMnO_3$-doped $BiFeO_3$ polycrystalline films on platinized substrates. The leakage current densities for 5% $LaMnO_3$-doped $BiFeO_3$ films was lower then pure BFO, however at higher doping content, the properties deteriorated. The 5%

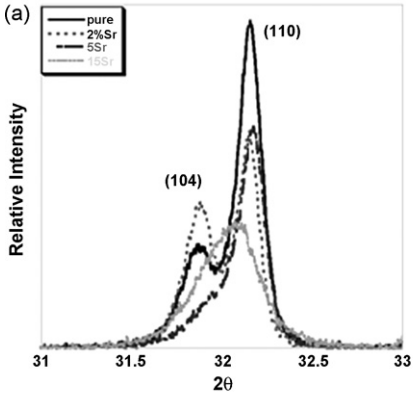

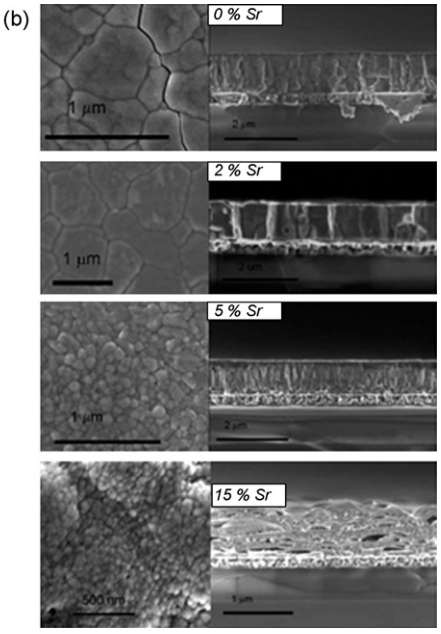

Fig. 11. (a) X- ray scan of the (1 0 4)/(1 1 0) spectral region, and (b) SEM determined microstructure: plane view and cross section pure BFO, 2% Sr, 5% Sr, and 15% Sr-doped $BiFeO_3$ films.
Figure was reproduced from Ref. [32], with permission of the copyright holders.

doped film showed well-saturated polarization loops with remanent polarization of 45 μC/cm^2 and coercive field of 215 kV/cm. The saturation magnetization for doped $BiFeO_3$ films was lower than that for pure $BiFeO_3$ films but increased with increasing $LaMnO_3$ content.

In order to improve the electrical resistivity, Yasui et al. fabricated 0–50% Sc-doped BFO films on Pt(1 1 1)/TiO_2/SiO_2/Si(1 0 0) substrates by CSD using $Bi(O^tC_5H_{11})_3$, $Fe(C_5H_7O_2)_3$, $Sc(O^iC_3H_7)_3$ [92,118]. The films had trace amounts of $Bi_2Fe_4O_9$ which increased with Sc^{3+} content. The variations in the d_{101} and d_{110} values with increasing Sc^{3+} content indicated that the ion substitution increased the *c*-axis as well as the *a*-axis. Well-saturated polarization hysteresis curves were observed for 15% Sc-doped BFO films (P_r = 35 μC/cm^2 and E_c = 295 kV/cm). The reduced leakage current density for 15% and 30% Sc^{3+}-doped BFO films (10^{-7} A/cm^2) compared to that of BFO film (10^{-4} A/cm^2) was attributed to the substitution of electrically unstable Fe^{3+} ions by Sc^{3+} cations. The effect of doping on magnetic properties was not investigated. In another independent study, $Bi(CH_3COO)_3$, $Fe(acac)_3$ and scandium nitrate were used for fabrication of 30% Sc-doped BFO films by sol–gel [87]. In this case too, the doping led to increase in unit cell volume (2%). The dielectric constant of the Sc-doped BFO film annealed in N_2 measured at 1 kHz was 235, compared to 208 for undoped BFO film. The films had a P_r value of 1.4 μC/cm^2 at 50 Hz. However, the increase in magnetization at room temperature was not significant.

Sakamoto et al. investigated $BiFeO_3$–$PbTiO_3$ thin films with near morphotropic phase boundary compositions [89,119]. $(1-x)BiFeO_3$–$xPbTiO_3$ (x = 0.2, 0.3, 0.4, 0.5) thin films (500 nm) were fabricated on platinized silicon substrates by chemical solution deposition using $Bi(O^tC_5H_{11})_3$, $Fe(OC_2H_5)_3$, $Pb(CH_3COO)_2$, and $Ti(O^iC_3H_7)_4$ as precursors. The deposited films crystallized in the perovskite phase and the stabilization in this phase was attributed to the formation of a solid solution with $PbTiO_3$. This was also claimed to cause reduction in oxygen ion vacancy which is usually observed due to high volatility of Bi and Pb. This was reflected in the electrical properties; the leakage current density was observed to decrease with increasing $PbTiO_3$ content. Due to defects leading to current leakages, well-saturated hysteresis curves were not observed for these films at room temperature. However, low-temperature measurements done at −190 °C led to observance of well-saturated hysteresis loops. $0.7BiFeO_3$–$0.3PbTiO_3$ exhibited the largest remanent polarization (P_r = 60 μC/cm^2, E_c = 230 kV/cm). Doping with Mn further improved the properties of BFO–PTO films and well-saturated hysteresis loops could be observed even at room temperature. In this case, it was suggested that the Mn^{2+} ions in the film could effectively trap the hopping electrons between Fe^{2+} and Fe^{3+}, a mechanism thought to be the main cause of leakage in $BiFeO_3$ films.

3.2.2.2. Laminates and other structures. In another approach to reduce the leakage currents in the $BiFeO_3$ films, Murari et al. used a 30 nm $Ba_{0.25}Sr_{0.75}TiO_3$ (BST) interlayer between the platinized substrate and 300 nm $BiFeO_3$ films [120]. The heterostructure was fabricated by chemical solution deposition. For the BST film, precursor solution prepared from barium(II) acetate trihydrate, strontium acetate and titanium isopropoxide was used. For the $BiFeO_3$ layer, bismuth(III) nitrate pentahydrate and iron 2–4 pentaniodinate were used as precursors. The $BiFeO_3$ films had rhombohedral crystal structure which was not affected by the BST interlayer. However, the BST interlayer affected the magnetization and electrical properties. The saturation magnetization and coercivity for the BFO/BST heterostructure was measured to be 19.6 emu cm^{-3} and 320 G, respectively which were slightly different from the values for pure BFO film (17.2 emu cm^{-3} and 346.5 G, respectively). The leakage current density for the heterostructure was reduced by three orders of magnitude, however the polarization hysteresis loops were weakly saturated.

Liu et al used a combination of modified sol–gel and electrochemical deposition processes to synthesize magnetoelectric $NiFe_2O_4$(NFO)-PZT core-shell nanowires [121]. The process consisted of three steps (Fig. 12): (i) using sol–gel to fabricate PZT nanotube in anodized aluminum oxide templates, (ii) forming a core-shell structure by filling the nanotubes with $Ni_{33}Fe_{67}$ alloy using electroplating, and (iii) oxidizing in air to obtain the NFO–PZT core-shell nanotube array. For the sol–gel step, a 0.3 M precursor solution with 10% excess lead content prepared by dissolving $Pb(CH_3CO_2)_2{\cdot}3H_2O$, $Zr(OCH_2CH_2CH_3)_4$ and $Ti(OC_4H_9)_4$ in 2-methoxyethanol was used. A saturation magnetization of 245 emu cm^{-3} and saturation polarization of 4 μC cm^{-2} was obtained. In a later report, they used another sol–gel process in which a mixed precursor solution was used to deposit $CoFe_2O_4$(CFO)-PZT nanocomposite films [122]. PZT precursor solution prepared by dissolving $Pb(CH_3CO_2)_2{\cdot}3H_2O$, $Zr(OCH_2CH_2CH_3)_4$ and $Ti(OC_4H_9)_4$ in 2-methoxyethanol was mixed in volume ratio 1:2 with CFO precursor solution prepared by dissolving $Co(CH_3CO_2)_2$ and $Fe(CH_3CO_2)_2{\cdot}3H_2O$ in 2-methoxyethanol. This solution was then used to deposit CFO–PZT nanocomposite films on $Ru/SiO_2/Si$ substrates. Perovskite PZT and spinel CFO phases were identified in XRD analysis. From the TEM analysis, well-defined

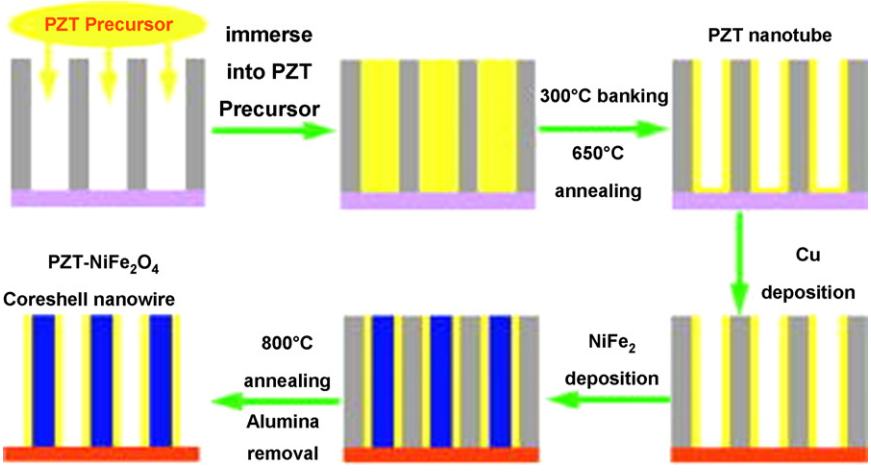

Fig. 12. Fabrication of NFO-PZT core-shell nanowires by modified sol–gel and electrochemical process. Figure was reproduced from Ref. [121], with permission of the copyright holders.

CFO grains surrounded by PZT grains were observed. This was attributed to the spontaneous phase separation during the short annealing of the spin-coated mixed precursor solution. The saturation magnetization of 118 emu cm^{-3} and polarization saturation of 18.5 $\mu C\,cm^{-2}$ was obtained.

4. Summary and conclusions

This review focused on the only two chemical synthesis routes that have been used for depositing thin multiferroic films. Both of these routes depend critically on the availability of suitable metalorganic precursors. The desirable properties of the precursors have been elucidated. For metalorganic chemical vapor deposition liquid precursors with sufficient volatility and good thermal stability are ideal. However, very few precursors satisfying these criteria are available for multiferroic materials. Since solid precursors have been the only option for most multiferroic materials, researchers have had to employ complex precursor delivery schemes which have been presented in the review. A variety of precursors and their combinations have been reported for the synthesis of multiferroic films by MOCVD as well as CSD techniques. Interestingly, different precursor combinations have resulted in thin films of the same material with significantly different properties. Therefore, there is a need to explore new precursor chemistries that would lead to optimal film properties. Development of novel tailored precursors would add flexibility in tuning the film properties which in general are dependant on the precursors and deposition process. Such an effort has proven to be critical to the progress of the complimentary metal oxide semiconductor and random access memory technologies in the microelectronic industry. A similar effort in the area of multiferroics holds great promise in taking us closer to the realization of the several proposed multifunctional devices. Availability of such precursors would facilitate the deposition of more complex structures that exhibit stronger multiferroic coupling than their single-phase counterparts.

Chemical vapor deposition route has been employed for depositing mainly single-phase multiferroic materials. The deposition of doped films and complex heterostructures by MOCVD is an area that is open for exploration subject to the availability of precursors that have good volatility and thermal stability. CSD routes have been used to synthesize single-phase materials, doped multiferroic materials as well as laminates with the latter two approaches being focused mainly on improving the current leakage properties. Again, the use of CSD for synthesizing multiferroic heterostructures is yet to be explored. A concerted effort between the synthesis chemists and materials scientists is required to expedite research in these areas.

Another critical effort is needed in carrying out fundamental studies such as in situ analysis to understand evaporation and reaction mechanisms of existing and new precursors during the deposition process. Such efforts would prove particularly important in designing metalorganic precursors.

Through five decades of continued research on magnetoelectric multiferroics a lot of progress has been made. A much better understanding of underlying mechanisms in single-phase as well as composites has been attained. New techniques with sub-nanometer level precision have been developed to fabricate multiferroic structures. Though we are getting closer to the point where devices based on such materials would be realized, this is still an area of basic research. Single-phase multiferroics thin films, particularly $BiFeO_3$ and $YMnO_3$, have received the most attention. Although through doping newer phases have been explored, the ordering temperatures are very low and the coupling effect in single-phase multiferroics is still too weak for device applications. Research efforts need to be directed towards the study of bilayered and multilayered epitaxial composites synthesized using techniques such as chemical vapor deposition, atomic layer deposition and chemical solution deposition that offer precise control over stoichiometry and microstructure along with the flexibility of using a wide variety of precursors and processing conditions. Through wide choice of materials constituting different layers, such composites also provide pathways to achieve strong coupling between ferroic properties above room temperature.

Acknowledgements

The authors are thankful to the National Science Foundation for providing funds under Grant # CMMI 0609377 for this study.

References

[1] K. Aizu, Phys. Rev. B 2 (1970) 754.
[2] H. Schmid, Ferroelectrics 162 (1994) 317.
[3] B.B. Van Aken, J.-P. Rivera, H. Schmid, M. Fiebig, Nature 449 (2007) 702.
[4] M. Fiebig, J. Phys. Appl. Phys. 38 (2005) R123.
[5] V.E. Wood, A.E. Austin, in: A.J. Freeman, H. Schmid (Eds.), Magnetoelectric Interaction Phenomena in Crystals, Gordon and Breach, London, 1975.
[6] *Scifinder Scholar*, version 2006, Chemical Abstracts Service, Columbus, OH, 2006 (accessed on December 9, 2008).
[7] I.E. Dzyaloshinskii, Zh. Eksp. Teor. Fiz. 37 (1959) 881.
[8] D.N. Astrov, Zh. Eksp. Teor. Fiz. 38 (1960) 984.
[9] N.A. Hill, J. Phys. Chem. B 104 (2000) 6694.
[10] N.A. Hill, A. Filippetti, J. Magn. Magn. Mater. 242–245 (2002) 976.
[11] C. Ederer, N.A. Spaldin, Curr. Opin. Solid State Mater. Sci. 9 (2006) 128.
[12] D.I. Khomskii, J. Magn. Magn. Mater. 306 (2006) 1.
[13] M.I. Bichurin, V.M. Petrov, G. Srinivasan, Phys. Rev. B 68 (2003) 054402.
[14] D.G. Schlom, J.H. Haeni, J. Lettieri, C.D. Theis, W. Tian, J.C. Jiang, X.Q. Pan, Mater. Sci. Eng. B 87 (2001) 282.
[15] W. Prellier, M.P. Singh, P. Murugavel, J. Phys. Condens. Matter 17 (2005) R803.
[16] W. Eerenstein, N.D. Mathur, J.F. Scott, Nature 442 (2006) 759.
[17] S.-W. Cheong, M. Mostovoy, Nat. Mater. 6 (2007) 13.
[18] R. Ramesh, N.A. Spaldin, Nat. Mater. 6 (2007) 21.
[19] L.D. Landau, E.M. Lifshitz, Electrodynamics of Continuous Media, Pergamon, Oxford, 1960.
[20] G.T. Rado, V.J. Folen, Phys. Rev. Lett. 7 (1961) 310.
[21] H. Schmid, Int. J. Magn. 4 (1973) 337.
[22] C. Ederer, N.A. Spaldin, Phys. Rev. B 71 (2005) 060401/1.
[23] R. Seshadri, N.A. Hill, Chem. Mater. 13 (2001) 2892.
[24] H. Wiegelmann, I.M. Vitebsky, A.A. Stepanov, A.G.M. Jansen, P. Wyder, Key Eng. Mater. 155–156 (1998) 429.
[25] B.I. Al'shin, D.N. Astrov, R.V. Zorin, Zh. Eksp. Teor. Fiz. 63 (1972) 2198.
[26] E. Ascher, H. Rieder, H. Schmid, H. Stoessel, J. Appl. Phys. 37 (1966) 1404.
[27] F. Kubel, H. Schmid, Acta Crystallogr. B 46 (1990) 698.
[28] C. Song, C.Z. Wang, Y.C. Yang, X.J. Liu, F. Zeng, F. Pan, Appl. Phys. Lett. 92 (2008) 262901.
[29] J.K. Kim, S.S. Kim, W.-J. Kim, A.S. Bhalla, R. Guo, Appl. Phys. Lett. 88 (2006) 132901.
[30] H. Uchida, R. Ueno, H. Funakubo, S. Koda, J. Appl. Phys. 100 (2006) 014106.
[31] X. Qi, J. Dho, R. Tomov, M.G. Blamire, J.L. MacManus-Driscoll, Appl. Phys. Lett. 86 (2005) 062903.
[32] K. Brinkman, T. Iijima, K. Nishida, T. Katoda, H. Funakubo, Ferroelectrics 357 (2007) 35.
[33] C. Dubourdieu, G. Huot, I. Gelard, H. Roussel, O.I. Lebedev, G. Van Tendeloo, Philos. Mag. Lett. 87 (2007) 203.
[34] J. Van den Boomgaard, A.M.J.G. Van Run, J. Van Suchtelen, Ferroelectrics 10 (1976) 295.
[35] J. Van den Boomgaard, R.A.J. Born, J. Mater. Sci. 13 (1978) 1538.
[36] J. Ryu, S. Priya, K. Uchino, H.-E. Kim, J. Electroceram. 8 (2002) 107.
[37] M.I. Bichurin, V.M. Petrov, G. Srinivasan, J. Appl. Phys. 92 (2002) 7681.
[38] K. Dorr, C. Thiele, J.W. Kim, O. Bilani, K. Nenkov, L. Schultz, Philos. Mag. Lett. 87 (2007) 269.
[39] G.B. Stringfellow, Organometallic Vapor-Phase Epitaxy: Theory and Practice, Academic Press, San Diego, CA, 1999.
[40] D.L. Smith, Thin-film Deposition: Principles and Practice, McGraw-Hill, New York, 1995.
[41] G.V. Bazuev, L.D. Kurbatova, Russ. Chem. Rev. 62 (1993) 981.
[42] K. Binnemans, in: K.A. Gschneidner, J.C. Bunzli, V.K. Pecharsky (Eds.), Handbook on the Physics and Chemistry of Rare Earths, vol. 35, Elsevier, 2005, p. 107.
[43] J.E. Sicre, J.T. Dubois, K.J. Eisentraut, R.E. Sievers, J. Am. Chem. Soc. 91 (1969) 3476.
[44] C. Bedoya, G.G. Condorelli, S.T. Finocchiaro, A. Di Mauro, I.L. Fragalà, L. Cattaneo, S. Carella, Chem. Vapor Depos. 11 (2005) 261.
[45] R. Ueno, S. Okaura, H. Funakubo, K. Saito, Jpn. J. Appl. Phys., Part 2 44 (2005) L1231.
[46] S.Y. Yang, F. Zavaliche, L. Mohaddes-Ardabili, V. Vaithyanathan, D.G. Schlom, Y.J. Lee, Y.H. Chu, M.P. Cruz, Q. Zhan, T. Zhao, R. Ramesh, Appl. Phys. Lett. 87 (2005) 102903.

[47] Y. Tasaki, T. Kanoko, M. Kabeya, N. Chifu, S. Yoshizawa, Integr. Ferroelectr. 81 (2006) 281.
[48] J. Thery, C. Dubourdieu, T. Baron, C. Ternon, H. Roussel, F. Pierre, Chem. Vapor Depos. 13 (2007) 232.
[49] M.S. Kartavtseva, O.Y. Gorbenko, A.R. Kaul, T.V. Murzina, S.A. Savinov, A. Barthélémy, Thin Solid Films 515 (2007) 6416.
[50] M.K. Singh, Y. Yang, C.G. Takoudis, A. Tatarenko, G. Srinivasan, P. Kharel, G. Lawes, Electrochem. Solid State Lett. 12 (2009) H161.
[51] K.-J. Choi, W.-C. Shin, S.-G. Yoon, Thin Solid Films 384 (2001) 146.
[52] A.A. Bosak, A.A. Kamenev, I.E. Graboy, S.V. Antonov, O.Y. Gorbenko, A.R. Kaul, C. Dubourdieu, J.P. Senateur, V.L. Svechnikov, H.W. Zandbergen, B. Holländer, Thin Solid Films 400 (2001) 149.
[53] D. Kim, D. Killingensmith, D. Dalton, V. Olariu, F. Gnadinger, M. Rahman, A. Mahmud, T.S. Kalkur, Mater. Lett. 60 (2006) 295.
[54] A.A. Bosak, C. Dubourdieu, J.P. Senateur, O.Y. Gorbenko, A.R. Kaul, J. Mater. Chem. 12 (2002) 800.
[55] I. Gelard, C. Dubourdieu, S. Pailhes, S. Petit, C. Simon, Appl. Phys. Lett. 92 (2008) 232506.
[56] T. Nakamura, R. Tai, K. Tachibana, J. Appl. Phys. 99 (2006) 08Q302/1.
[57] Y. Kojima, H. Kadokura, Y. Okuhara, M. Matsumoto, T. Mogi, Integr. Ferroelectr. 18 (1997) 183.
[58] Y. Tasaki, J. Ishiai, S. Yoshizawa, Y. Kuniya, Nippon Kagaku Kaishi (1999) 45.
[59] M.A. Siddiqi, B. Atakan, J. Chem. Eng. Data 51 (2006) 1092.
[60] A.C. Jones, M.L. Hitchman, Chemical Vapour Deposition: Precursors, Processes and Applications, Royal Society of Chemistry, Cambridge, UK, 2009.
[61] M.A.V. Ribeiro da Silva, M.J.S. Monte, J. Huinink, J. Chem. Thermodyn. 28 (1996) 413.
[62] M. Fulem, K. Ruzicka, V. Ruzicka, T. Simecek, E. Hulicius, J. Pangrác, J. Cryst. Growth 264 (2004) 192.
[63] S. Yuhya, K. Kikuchi, M. Yoshida, K. Sugawara, Y. Shiohara, Mol. Cryst. Liq. Cryst. 184 (1990) 231.
[64] L. Niinistö, J. Therm. Anal. Calorim. 56 (1999) 7.
[65] G. Malandrino, Z. Lipani, R.G. Toro, M.E. Fragalà, Inorg. Chim. Acta 361 (2008) 4118.
[66] T. Furukawa, N. Oshima, M. Suzuki, S. Okaura, H. Funakubo, Integr. Ferroelectr. 84 (2006) 197.
[67] P.A. Williams, A.C. Jones, N.L. Tobin, P.A. Marshall, P.R. Chalker, H.O. Davies, L.M. Smith, Mater. Res. Soc. Symp. Proc. 748 (2003) 105.
[68] A.C. de Souza, A.T.N. Pires, V. Soldi, J. Therm. Anal. Calorim. 70 (2002) 405.
[69] M.K. Singh, Y. Yang, C.G. Takoudis, J. Electrochem. Soc. 155 (2008) D618.
[70] Y.-Y. Wang, Y.-Z. Jiang, J.-F. Gao, M.-F. Liu, G.-Y. Meng, Wuji Huaxue Xuebao 22 (2006) 1269.
[71] K.J. Eisentraut, R.E. Sievers, J. Inorg. Nucl. Chem. 29 (1967) 1931.
[72] G. Garcia, J. Casado, J. Llibre, A. Figueras, J. Cryst. Growth 156 (1995) 426.
[73] R.L. Nigro, R.G. Toro, G. Malandrino, I.L. Fragala, P. Rossi, P. Dapporto, J. Electrochem. Soc. 151 (2004) F206.
[74] M. Leskelä, L. Niinistö, E. Nykänen, P. Soininen, M. Tiitta, Thermochim. Acta 175 (1991) 91.
[75] J. Päiväsaari, M. Putkonen, T. Sajavaara, L. Niinistö, J. Alloys Compd. 374 (2004) 124.
[76] R. Amano, A. Sato, S. Suzuki, Bull. Chem. Soc. Jpn. 54 (1981) 1368.
[77] R.W. Schwartz, T. Schneller, R. Waser, Compt. Rendus Chem. 7 (2004) 433.
[78] C.J. Brinker, G.W. Scherer, Sol–Gel Science: The Physics and Chemistry of Sol–Gel Processing, Academic Press, Boston, 1990.
[79] R.W. Schwartz, Chem. Mater. 9 (1997) 2325.
[80] S. Iakovlev, C.H. Solterbeck, M. Kuhnke, M. Es-Souni, J. Appl. Phys. 97 (2005) 094901.
[81] C.-F. Chung, J.-P. Lin, J.-M. Wu, Appl. Phys. Lett. 88 (2006) 242909.
[82] S. Yakovlev, J. Zekonyte, C.H. Solterbeck, M. Es-Souni, Thin Solid Films 493 (2005) 24.
[83] C.-F. Chung, J.-M. Wu, Electrochem. Solid State Lett. 8 (2005) F63.
[84] S. Habouti, C.H. Solterbeck, M. Es-Souni, J. Sol–Gel Sc. Technol. 42 (2007) 257.
[85] S. Habouti, C.H. Solterbeck, M. Es-Souni, J. Appl. Phys. 102 (2007) 074107.
[86] X. Qi, J. Dho, M. Blamire, Q. Jia, J.-S. Lee, S. Foltyn, J.L. MacManus-Driscoll, J. Magn. Magn. Mater. 283 (2004) 415.
[87] S.R. Shannigrahi, A. Huang, D. Tripathy, A.O. Adeyeye, J. Magn. Magn. Mater. 320 (2008) 2215.
[88] T. Sun, H. Hu, Z. Pan, X. Li, J. Wang, V.P. Dravid, Phys. Rev. B 77 (2008) 205414.
[89] W. Sakamoto, A. Iwata, T. Yogo, J. Appl. Phys. 104 (2008) 104106.
[90] S.K. Singh, K. Maruyama, H. Ishiwara, J. Phys. Appl. Phys. 40 (2007) 2705.
[91] F. Tyholdt, S. Jorgensen, H. Fjellvag, A.E. Gunnaes, J. Mater. Res. 20 (2005) 2127.
[92] S. Yasui, H. Uchida, H. Nakaki, K. Nishida, H. Funakubo, S. Koda, Appl. Phys. Lett. 91 (2007) 022906.
[93] Y. Nakamura, S. Nakashima, D. Ricinschi, M. Okuyama, Mater. Res. Soc. Symp. Proc. 1034E (2008) Paper #: 1034K1110.
[94] G. Teowee, K.C. McCarthy, F.S. McCarthy, T.J. Bukowski, D.G. Davis, D.R. Uhlmann, J. Sol–Gel Sci. Technol. 13 (1998) 899.
[95] H. Kitahata, K. Tadanaga, T. Minami, N. Fujimura, T. Ito, J. Sol–Gel Sci. Technol. 19 (2000) 589.
[96] K.-T. Kim, C.-I. Kim, J. Eur. Ceram. Soc. 24 (2004) 2613.
[97] H. Kitahata, K. Tadanaga, T. Minami, N. Fujimura, T. Ito, Jpn. J. Appl. Phys., Part 1 38 (1999) 5448.
[98] W.-C. Yi, J.-S. Choe, C.-R. Moon, S.-I. Kwun, J.-G. Yoon, Appl. Phys. Lett. 73 (1998) 903.
[99] W.-C. Yi, C.-S. Seo, S.-I. Kwun, J.-G. Yoon, Appl. Phys. Lett. 77 (2000) 1044.
[100] K. Suzuki, K. Nishizawa, T. Miki, K. Kato, J. Cryst. Growth 237–239 (2002) 482.
[101] G. Westin, K. Jansson, Adv. Sci. Technol. (Faenza, Italy) 17 (1999) 211.
[102] J.P. Sénateur, F. Felten, S. Pignard, F. Weiss, A. Abrutis, V. Bigelyte, A. Teiserskis, Z. Saltyte, B. Vengalis, J. Alloys Compd. 251 (1997) 288.
[103] A.R. Kaul, B.V. Seleznev, J. Phys. IV France 3 (1993) 375.
[104] A.A. Bossak, I.E. Graboy, O.Y. Gorbenko, A.R. Kaul, M.S. Kartavtseva, V.L. Svetchnikov, H.W. Zandbergen, Chem. Mater. 16 (2004) 1751.
[105] T. Nakamura, K. Homma, T. Yakushiji, R. Tai, A. Nishio, K. Tachibana, Surf. Coat. Technol. 201 (2007) 9275.
[106] T. Nakamura, K. Homma, R. Tai, A. Nishio, K. Tachibana, IEEE Trans. Magn. 43 (2007) 3070.
[107] H. Itoh, T. Uemura, H. Yamaguchi, S. Naka, J. Mater. Sci. 24 (1989) 3549.
[108] E. Fujii, H. Torii, R. Takayama, T. Hirao, Jpn. J. Appl. Phys. Part 1 34 (1995) 130.
[109] M. Langlet, J.L. Deschanvres, M. Labeau, J.C. Joubert, Magn. Thin Films (1986) 107.
[110] T. Schneller, R. Waser, Ferroelectrics 267 (2002) 293.
[111] J.F. Scott, F.D. Morrison, M. Miyake, T. Tatsuta, O. Tsuji, Key Eng. Mater. 333 (2007) 71.
[112] F. Tyholdt, H. Fjellvag, A.E. Gunnaes, A. Olsen, J. Appl. Phys. 102 (2007) 074108.
[113] X. Qi, P.S. Roberts, N.D. Mathur, J.S. Lee, S. Foltyn, Q.X. Jia, J.L. MacManus-Driscoll, Ceram. Trans. 162 (2005) 69.
[114] F. Bai, J. Wang, M. Wuttig, J. Li, N. Wang, A.P. Pyatakov, A.K. Zvezdin, L.E. Cross, D. Viehland, Appl. Phys. Lett. 86 (2005) 032511.
[115] Y. Nakamura, S. Nakashima, M. Okuyama, Jpn. J. Appl. Phys. 47 (2008) 7250.
[116] K. Tadanaga, H. Kitahata, T. Minami, N. Fujimura, T. Ito, J. Sol–Gel Sci. Technol. 13 (1998) 903.
[117] K. Suzuki, D. Fu, K. Nishizawa, T. Miki, K. Kato, Integr. Ferroelectr. 52 (2003) 55.
[118] S. Yasui, H. Uchida, H. Nakaki, H. Funakubo, S. Koda, Jpn. J. Appl. Phys. 45 (2006) 7321.
[119] W. Sakamoto, H. Yamazaki, A. Iwata, T. Shimura, T. Yogo, Jpn. J. Appl. Phys. Part 1 45 (2006) 7315.
[120] N.M. Murari, A. Kumar, R. Thomas, R.S. Katiyar, Appl. Phys. Lett. 92 (2008) 132904.
[121] M. Liu, X. Li, H. Imrane, Y. Chen, T. Goodrich, Z. Cai, K.S. Ziemer, J.Y. Huang, N.X. Sun, Appl. Phys. Lett. 90 (2007) 152501.
[122] M. Liu, X. Li, J. Lou, S. Zheng, K. Du, N.X. Sun, J. Appl. Phys. 102 (2007) 083911.